


**RESEARCH ARTICLE**

# Local and non-local controls on a persistent cold-air pool in the Arve River Valley

G. Arduini<sup>1,2</sup>  | C. Chemel<sup>1,3</sup> | C. Staquet<sup>2</sup>

<sup>1</sup>Centre for Atmospheric and Instrumentation Research, University of Hertfordshire, Hatfield, UK

<sup>2</sup>Université Grenoble Alpes, CNRS, LEGI, Grenoble France

<sup>3</sup>National Centre for Atmospheric Science, University of Hertfordshire, Hatfield, UK

**Correspondence**

Gabriele Arduini, European Centre for Medium-Range Weather Forecasts, Reading RG2 9AX, UK.  
Email: gabriele.arduini@ecmwf.int

**Funding information**

LabEx OSUG@2020 Investissements d'avenir, Grant/Award Number: ANR10LABX56

**Abstract**

A numerical model is used to simulate a persistent cold-air pool (PCAP) event that occurred in the section of the Arve River Valley around Passy in the French Alps. During this period, an upper-level ridge from the Atlantic moved over Europe, allowing a PCAP to form and persist over time. The impact of the upper-level ridge on the PCAP and on the dynamics within the valley section is quantified by examining the mass and heat budgets of the valley atmosphere. During the persistent stage, the magnitude of the flow through the tributary valleys is enhanced by the large-scale flow. Also, the direction of the flow through one of the tributaries is found to be determined by the height of the PCAP with respect to that of the tributary above the valley floor. The tributary flows, together with subsiding motions at the valley top, control by and large the night-time valley-scale circulation and the thermal structure of the upper part of the PCAP, whereas thermally driven valley flows control its lower part. When the upper-level ridge passes over the Arve River Valley, warm air advection through the tributaries continuously erodes the upper part of the PCAP during night-time, thereby reducing its depth, while down-valley flows export the air mass out of the valley. As the ridge moves away from the valley, the near-surface air is found to be trapped within the valley. This trapping results from the advection of warm air in the upper part of the PCAP by the large-scale flow channelled through one of the tributaries. This reduces the thermally induced pressure difference in the down-valley direction, thereby suppressing the near-surface down-valley flow. The study therefore highlights the interplay between the large-scale flow, the tributary flows and the thermal structure of the PCAP.

**KEYWORDS**

cold-air pool, complex terrain, PASSY-2015, stable boundary layer

## 1 | INTRODUCTION

A cold-air pool (CAP) is a stably stratified layer of air confined at the bottom of a valley or basin. Diurnal CAPs form frequently during nocturnal hours under clear-sky and weak synoptic wind conditions and are destroyed following sunrise mainly by convection resulting from surface heating. When relatively warm air associated with anticyclonic conditions is transported right above deep terrain over multiple days (Reeves and Stensrud, 2009), convection is often insufficient to destroy the stable layer within the valley, particularly during wintertime (e.g., Vrhovc and Hrabar, 1996; Lu and Zhong, 2014), allowing a persistent cold-air pool (PCAP) to develop. Since a PCAP is characterised by a long-lasting (multi-day) valley inversion and weak winds, air pollutants and moisture emitted within the PCAP are trapped and accumulate from day to day, thereby affecting air quality (Silcox *et al.*, 2012; Chemel *et al.*, 2016; LARGERON and Staquet, 2016a) and visibility when fog forms. The removal of the PCAP may occur because of the passage of a synoptic disturbance over the valley (Zhong *et al.*, 2001), turbulent erosion of the PCAP from the top (LAREAU and Horel, 2015a) or the displacement of the cold-air layer out of the valley (Flamant *et al.*, 2006; LAREAU and Horel, 2015b). While the formation, persistence and destruction stages are common to PCAPs in many different regions and conditions (Zhong *et al.*, 2001; ZÄNGL, 2005a; LAREAU *et al.*, 2013; Lu and Zhong, 2014; LARGERON and Staquet, 2016b), the characteristics of the PCAP (depth and strength) during each stage depend on the characteristics of the surrounding terrain and variability of the synoptic conditions. Thereafter, a distinction is made between the processes that control the characteristics of the PCAP and are governed by those of the terrain at the valley or basin scale, which are referred to as *local* controls (such as local thermally driven flows), and processes affecting the PCAP characteristics but occurring at scales larger than that of the valley (such as the synoptic wind above the valley boundary layer and flows from surrounding tributary valleys modified by the large-scale flow), which are referred to as *non-local* controls.

Previous work has considered local controls on CAPs. Vrhovc (1991) showed using results from numerical simulations of a diurnal CAP in the Slovenj Gradec basin that a dynamical decoupling can take place between the flow within the valley boundary layer and the synoptic flow aloft. As a result, at the top of a CAP an abrupt change in wind speed and direction was observed. In such decoupled conditions, thermally driven along-slope and along-valley flows are the key dynamical features of the valley atmosphere (LARGERON and Staquet, 2016a). However, much remains to be understood on their role in the formation and evolution of CAPs (BODINE *et al.*, 2009). In a numerical

modelling case-study of the formation of a CAP in a  $\sim 100$  m deep narrow valley, Vosper *et al.* (2014) concluded that the principal mechanism responsible for the formation of the CAP was the sheltering effect of the valley. The sheltering was shown to increase the turbulent heat flux divergence close to the ground compared to a less sheltered region (i.e., hilltop sites), thereby increasing near-surface cooling and promoting the formation of a ground-based inversion. However, in such a shallow valley, thermally driven flows are rapidly suppressed after the evening transition (Clements *et al.*, 2003; Vosper *et al.*, 2014). In a deep and narrow valley dynamically decoupled from the atmosphere above, downslope flows can persist for a longer time, reaching a quasi-steady state if a down-valley flow can develop during the night (Burns and Chemel, 2015; Arduini *et al.*, 2016). Under these conditions, downslope flows are the main driver of the sensible heat flux divergence, which enhances the cooling of the atmosphere in the valley with respect to a flat region nearby. Downslope flows are also important in the evolution of the thermal structure of the upper part of a CAP, through the vertical transport induced by the air flowing down the slopes (Whiteman, 1982; Kiefer and Zhong, 2011; Burns and Chemel, 2015; Arduini *et al.*, 2016).

In addition to thermally driven flows, the variations of the orography and surface properties affect the evolution of a CAP. Because of the reduction in the volume of atmosphere in a valley or basin when compared to that over a flat terrain, a valley or basin experiences a cooling that is stronger than if it were a flat terrain for the same amount of heat loss (Whiteman, 1990). A differential cooling can also take place between different sections of the same valley because of along-valley geometrical variations (McKee and O'Neal, 1989). This differential cooling can lead to along-valley flows that are up-valley instead of down-valley during the night (Arduini *et al.*, 2017), affecting the mass and heat budgets of the valley atmosphere. If the ground is covered by snow (as is common in winter in alpine regions), surface albedo is increased and the heat conductivity to the ground is significantly decreased, leading to stronger ground-based inversions (ZÄNGL, 2005b; Billings *et al.*, 2006; Neemann *et al.*, 2015).

Non-local controls on PCAPs have been examined for a number of case-studies. Zhong *et al.* (2001) showed that the formation and maintenance of a PCAP event in the Columbia basin in the Pacific Northwest region of North America was primarily the result of the continuous advection of warm air immediately above the basin by strong westerly winds descending the lee slopes of the surrounding Cascade mountains. Similar results regarding the importance of large-scale advection of warm air above the terrain in the formation and maintenance of a PCAP in the Salt Lake Valley, Utah, USA, were reported

by Wei *et al.* (2013). Lu and Zhong (2014) quantified the respective contributions of the different terms determining the heat budget of the atmosphere during this PCAP event. Large-scale advection was found key to the formation, maintenance and destruction of the PCAP.

While these studies have demonstrated the essential role of warm air advection in the formation and maintenance of a PCAP, the dynamical controls of large-scale flows on the temporal evolution of CAPs have received less attention. In a numerical modelling case-study, Zängl (2005a) showed the importance of the direction of the synoptic pressure gradient and of the along-valley terrain geometry, with respect to the Alpine foreland, in the maintenance of CAPs in a deep Alpine valley system. Model results indicated that the direction of the synoptic pressure gradient controlled the direction of the along-valley drainage flows. The author concluded that, for that particular case-study, the ideal conditions for the removal of a CAP are met when the synoptic pressure gradient is orientated down a constriction in the along-valley direction. In a following work based on semi-idealised numerical simulations and observations, Zängl (2005c) extended this analysis to the shallower Bavarian Danube basin. Model results showed that advection resulting from the synoptic pressure difference (pressure-driven channelling) and advection down the direction of the synoptic wind (forced-channelling) can both act to remove the PCAP, depending on the direction of the synoptic wind with respect to the orientation of the highest mountain range. Another dynamical mechanism which may affect the temporal evolution of PCAPs is shear-induced turbulent mixing at the top of the PCAP due to strong winds aloft. Some studies questioned the effectiveness of such turbulent erosion for the destruction of CAPs over time-scales shorter than one day (e.g., Zhong *et al.*, 2001; Zhong *et al.*, 2003). However, semi-idealised numerical simulations analysed by Zängl (2005c) suggested that this mechanism can contribute significantly to the destruction of a CAP in the relatively shallow Danube basin. In deep valleys, idealised simulations by Lareau and Horel (2015a) indicated that CAPs can be removed by turbulent erosion on a time-scale of less than a day, provided that the speed of the flow aloft increases continuously with time such that the Froude number exceeds a threshold value of about 2. A more systematic study on the link between the size of the valley and the synoptic conditions has been performed by Sheridan (2019) by means of idealised 2D simulations. The author showed that for deep (~1,000 m) valleys embedded within a plateau, for increasing background stability, the CAP becomes increasingly more sheltered from the external flow and so more prone to being persistent. This behaviour was found to be well described by a non-dimensional valley-depth

parameter (Vosper and Brown, 2008). However, in the case of a valley embedded between two hills – a more common situation in the Alpine environment – the relationship between the non-dimensional valley depth and CAP persistency was found to be more complex, and a very strong background stability (in a real case associated for instance with synoptic warm air advection) was required to maintain the CAP persistent in time.

The contribution of tributary flows in the mass budget of a valley was studied extensively as part of the Advanced Studies in Complex Terrain (ASCOT) programme (Clements *et al.*, 1989). However, the computation of mass fluxes through tributaries relied solely on limited observations, and so several assumptions and approximations had to be made to estimate their contributions to the mass budget. Porch *et al.* (1989) calculated that the mass flux through a single tributary may account for 5 to 15% of the drainage out of Brush Creek Valley, Colorado, USA. Assuming a similar contribution from all the tributaries of Brush Creek Valley, the authors estimated that tributary flows control by and large the mass budget of the valley, and so that the contribution of slope flows and subsiding motions at the valley top are only minor. Numerical model simulations reported by O'Steen (2000) for an idealised valley-tributary system under dynamically decoupled conditions confirmed that the flow through the tributary can increase the along-valley mass flux by 5 to 10% compared to an idealised valley without a tributary. However, some of the complex interactions between the tributary flow and the down-valley flow were not captured with this idealised configuration. Coulter *et al.* (1989) showed that the mass flux through the tributary is extremely sensitive to the external flow. Under particular synoptic conditions, the drainage from the tributary was found to be 20% larger than that expected if the mass flux was assumed proportional to the drainage area. Coulter *et al.* (1991) examined the mass fluxes through three tributaries of Kimball Creek, Colorado, and showed that the mass flux is largest for the tributary most closely aligned with the valley axis. Despite the efforts of the ASCOT programme, large uncertainties remain about the effects of tributary flows on the heat and mass budget of a valley atmosphere.

In this paper, we investigate the role of local and non-local controls, the latter including the synoptic wind above the valley boundary layer and flows from the surrounding tributary valleys affected by the large-scale flow, in the evolution of a PCAP using numerical model simulations. The PCAP event occurred in the section of the Arve River Valley around Passy in the French Alps, in February 2015, during the first intensive observation period (IOP1) of the PASSY-2015 field campaign (Staquet *et al.*, 2015; Paci *et al.*, 2016). To reach this aim, the mass and heat

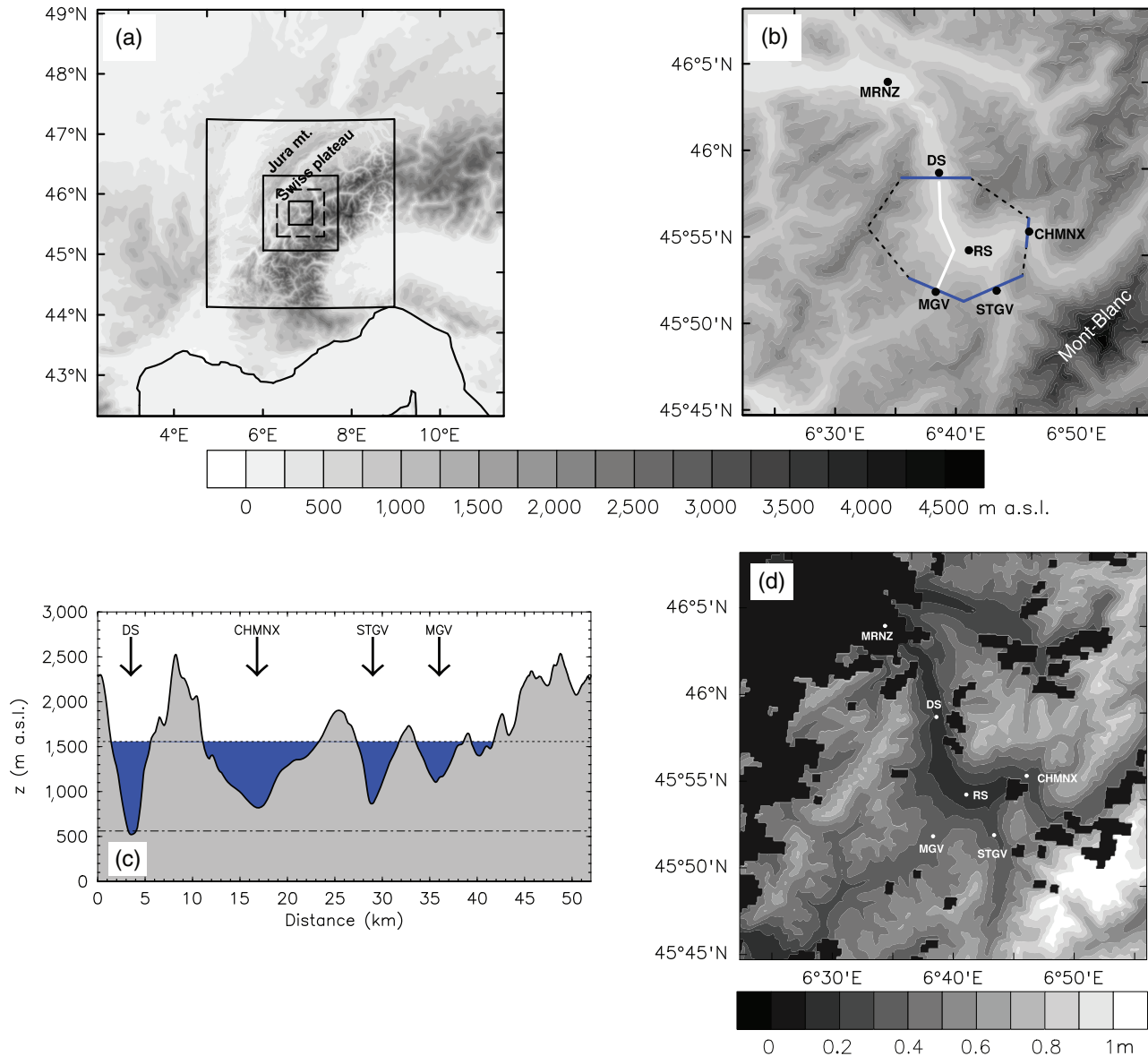


**FIGURE 1** (a) Topographic map of domain d02 with the positions of the nested domains d03, d04 and d05, represented by continuous-line boxes. The dashed-line box represents the region covered by the semi-idealised simulation, WRF-I. (b) Topographic map of the innermost domain d05. The dashed black polygon indicates the horizontal extent of the PASSY control volume, the white line indicates the path of cross-sections used in the paper, and mass and heat fluxes are calculated across "gates" represented by the blue lines. The position of selected sites are labelled: radio soundings (RS), downstream part of the valley (DS), Megève (MGV), Saint-Gervais-les-Bains (STGV), Chamonix (CHMNX) and Marnaz (MRNZ). (c) Terrain height around the polygon defining the PASSY control volume. The dotted line indicates the mean height of the terrain along the polygon and the dashed-dotted line is the height of the RS site; see text for further details. (d) Snow depth in the innermost domain d05 at 1200 UTC on 8 February 2015; the position of selected sites are labelled in bold as in (b)

budgets in the Passy valley are analysed and compared to the ones for a semi-idealised simulation in which the synoptic flow in the initial condition is at rest. In Section 2, we present the design of the numerical simulations. Section 3 provides an overview of the synoptic conditions during IOP1. A detailed description of the episode and the evaluation of model data with field observations are reported in Section 4. Model results are analysed in Sections 5 and 6. A summary and conclusions are presented in Section 7.

## 2 | METHODOLOGY

### 2.1 | The Passy Valley

The Arve River Valley is located in the French Alps to the south of the Jura mountain range and the Swiss Alps (Figure 1a). Hereafter the Passy Valley refers to the section of the Arve River Valley enclosed by the dashed black

polygon in Figure 1b. The mean height of the terrain along the polygon defining the PASSY control volume is  $z_m = 1,560$  m a.s.l. (Figure 1c), and the highest massif surrounding the Arve River Valley is Mont Blanc, culminating at 4,808 m a.s.l. (above sea level). The valley-floor elevation decreases gradually down-valley from 588 m a.s.l. at Passy (upstream of the radio sounding (RS) site) to 488 m a.s.l. at Marnaz (MRNZ) over a distance of about 23 km. The width of the valley floor along this section of the valley increases gradually up-valley from just about 200 m upstream of MNRZ, where the valley presents a major constriction, to approximately 2,000 m near the location of the RS site, and hardly decreases from there towards the escarpment leading to Chamonix (CHMNX). In the context of this work, the section of the Arve River Valley leading to CHMNX is considered a tributary of the Passy Valley. Therefore, the Passy valley presents three major tributaries leading to Megève (MGV), Saint-Gervais-les-Bains (STGV) and CHMNX (Figure 1c).

## 2.2 | Terrain representation and snow initialisation

An accurate representation of the terrain is essential to numerical modelling in complex terrain such as Alpine valley systems. Most Alpine valleys are characterised by steep slopes which are a challenge for numerical models formulated using terrain-following coordinates, as is the case for the Weather Research and Forecasting (WRF) model used here. Even using a horizontal mesh size of the order of 3 km, slope angles exceed  $25^\circ$  across the Alpine chain of western Europe. With a horizontal mesh size of 100 m, the maximum slope angle in the Arve River Valley is about  $75^\circ$ . In the present work, 90 m terrain elevation data from the Shuttle Radar Topography Mission (SRTM; Farr *et al.*, 2007) were interpolated at the horizontal mesh size of the nested model domains (Figure 1a). A smoothing filter was used to reduce the largest slope angles of the terrain to a maximum slope angle  $\alpha_{\max} = 45^\circ$  while minimising any changes in the overall shape and small-scale features of the valley geometry.

Several studies have pointed out that the presence of snow on the ground surface significantly alters surface–atmosphere interactions (Zängl, 2005b; Neemann *et al.*, 2015; Tomasi *et al.*, 2017). The initialisation and modelling of the snowpack are difficult tasks. Numerical model analysis products are currently available at too coarse a resolution ( $\sim 15$  km) to be used to provide an appropriate representation of the snow cover at sub-kilometre scales. Furthermore, the initialisation of the snow density performed by the WRF Preprocessing System (WPS) assumes climatological values that are not representative

for a specific case-study. In the present work, MODIS/Terra (MOD10\_L2) satellite products at a spatial resolution of 500 m (Hall *et al.*, 2006) were used to initialise snow cover and albedo. The snow mask was directly interpolated at the horizontal grid points of the nested model domains. To initialise snow albedo, we followed the methodology outlined by Tomasi *et al.* (2017). Snow albedo is a function of the age of the snow (Livneh *et al.*, 2010), which is initialised as fresh snow (i.e., with the largest value for snow albedo, based on an analysis of climatological data; Robinson and Kukla, 1985). A snow age corresponding to the satellite-retrieved albedo was calculated by inverting the functional relationship proposed by Livneh *et al.* (2010), which is implemented in the current version of the Noah land-surface model. The calculated snow age was then used as initial condition. The snow water equivalent was diagnosed by assuming that the density of the snow is, as a zero-order approximation, only a function of the age of the snow (Meløysund *et al.*, 2007). Hence, given the snow depth, the snow water equivalent can be specified at the initial time. Snow depth was assumed to depend only on the elevation of the underlying terrain, as in previous studies (e.g., Schmidli *et al.*, 2009). Snow depth was initialised to increase linearly with height from a value of 0.05 m at sea level to 0.15 m at 500 m a.s.l., and to 1.5 m at 4,500 m a.s.l. (Figure 1d).

## 2.3 | Model set-up

The numerical simulations were performed using the WRF model with the advanced research core (ARW; Skamarock *et al.*, 2008), version 3.5.1. Five nested domains were used (Table 1 gives the spatial and temporal resolutions used for the domains). The simulations were performed in three steps.

Firstly, a simulation for the three outermost domains (d01, d02 and d03) was performed using online one-way nesting and a grid ratio of 5 and 3 for domains d02 and d03, respectively. The computations were made on 46 vertical layers. The grid was stretched along the vertical axis, with a vertical spacing of about 40 m near the ground surface (so that the first mass point above the surface is approximately at 20 m). The use of a relatively low vertical resolution in the outermost domains was required to keep the model numerically stable and the simulated terrain height as close as possible to the real orography. Lateral boundary conditions for d02 and d03 were updated every parent domain time step. Initial conditions other than those for the snow fields and lateral boundary conditions for the outermost domain d01 were derived from the European Centre for Medium-range Weather Forecasts (ECMWF) gridded analyses available

**TABLE 1** Spatial and temporal resolutions for the domains used for the real-case numerical simulations: number of points  $n_x$ ,  $n_y$  and  $n_z$  in the east, north and vertical directions, respectively, horizontal mesh size  $\Delta x = \Delta y$ , vertical grid spacing near the ground surface  $\Delta z_{\min}$ , time step  $\Delta t$  and frequency  $f_{\text{bu}}$  at which the lateral boundaries of the nested grids were updated

Domain	$n_x, n_y, n_z$	$\Delta x = \Delta y$	$\Delta z_{\min}$ (m)	$\Delta t$ (s)	$f_{\text{bu}}$
d01	202, 202, 46	15 km	42	30	6 hr
d02	246, 246, 46	3 km	42	6	30 s
d03	340, 340, 46	1 km	42	2	6 s
d04	406, 406, 92	333 m	21	0.6	10 min
d05	382, 382, 92	111 m	21	0.1	5 min

every 6 hr with a horizontal mesh size of  $0.25^\circ$ . The simulation was run continuously for 7 days from 7 to 14 February 2015. To minimise the deviation of the model results from the ECMWF analyses, spectral nudging was used for d01 and d02. Only the upper part of domain d03 (above 6000 m a.s.l.) was nudged towards the analyses. Snow cover and albedo were initialised from MODIS/Terra (MOD10\_L2) satellite products (see Section 2.2) averaged in time between 5 and 10 February 2015.

Secondly, a simulation for domain d04 was performed using initial and lateral boundary conditions extracted from the results for d03, using offline nesting. The extent of d04 was chosen to cover the main regional-scale orographic feature surrounding the Passy Valley (Figure 1a). The horizontal mesh size was set to 333 m and the number of vertical levels increased to 92, compared to the outermost domains, with a vertical mesh size of about 20 m near the ground surface (so that the first mass point above the surface is approximately at 10 m) and 29 levels in the lowest 1,000 m above the surface. The lateral boundary conditions were updated every 10 min. This simulation was run continuously from 8 to 14 February 2015.

Finally, a simulation for domain d05 was performed using a methodology similar to that used for domain d04. Differences are that the lateral boundary conditions were updated every 5 min to minimise spurious effects at these boundaries. Also, this simulation was reinitialised every day at 1200 UTC to facilitate the comparison with semi-idealised simulations (discussed below). The coverage of d05 is shown in Figure 1b. The number of vertical levels was the same as that of d04, but the horizontal grid mesh size used was refined to 111 m. Results from additional sensitivity simulations revealed negligible differences when a domain size twice as large as that of d05 is used. Results from this sensitivity study also showed that a horizontal mesh size as fine as 111 m was required to resolve the constriction in the downstream part of the Passy valley. The constriction is closed for a coarser resolution which was found to significantly modify the dynamics of the near-surface valley atmosphere (not shown).

The simulation for d05 is the reference simulation and is referred to as WRF-R hereafter.

All nested domains were centred at the airport in Sallanches ( $45.935^\circ\text{N}$ ,  $6.636^\circ\text{E}$ ) and shared the same “dynamics” and “physics” options, apart from that for the planetary boundary layer (PBL) and subgrid-scale turbulence. A third-order Runge–Kutta scheme was used to integrate the model equations and a time-splitting technique was used to integrate the acoustic modes. The advection terms were discretised using a fifth-order Weighted Essentially Non-Oscillatory (WENO) scheme with positive definite filter. The PBL was parametrized for d01, d02 and d03 using the Yonsei University (YSU) parametrization scheme (Hong, 2010). In the higher-resolution simulations for d04 and d05, a 3D turbulent kinetic energy (TKE) diffusion scheme is used (and no PBL scheme), modified to enable the gravitational settling of fog, following the formulation proposed by Nakanishi (2000). Land surface processes were modelled using the Noah land surface model (Chen and Dudhia, 2001) using four soil layers. A few modifications of the land surface model from the WRF model version 3.7 were implemented in the model used in the present work. These are the computation of the ground thermal conductivity (to prevent a discontinuous behaviour during the melting of frozen water in the soil), and the calculation of the latent heat flux (to take into account dew deposition processes over snow-covered surfaces). The Monin–Obukhov similarity theory (Jiménez *et al.*, 2012) is used to couple the land surface to the atmosphere.

Short-wave and long-wave radiation were parametrized using the Rapid Radiative Transfer Model (Mlawer *et al.*, 1997). Shadowing effects were included to take into account the effect of the mountains on the radiative fluxes. The microphysics were parametrized using the scheme developed by Morrison *et al.* (2005), modified for the treatment of ice fog following Neemann *et al.* (2015). The number of cloud condensation nuclei was increased to  $500 \times 10^6$ , a value more representative of continental environments.

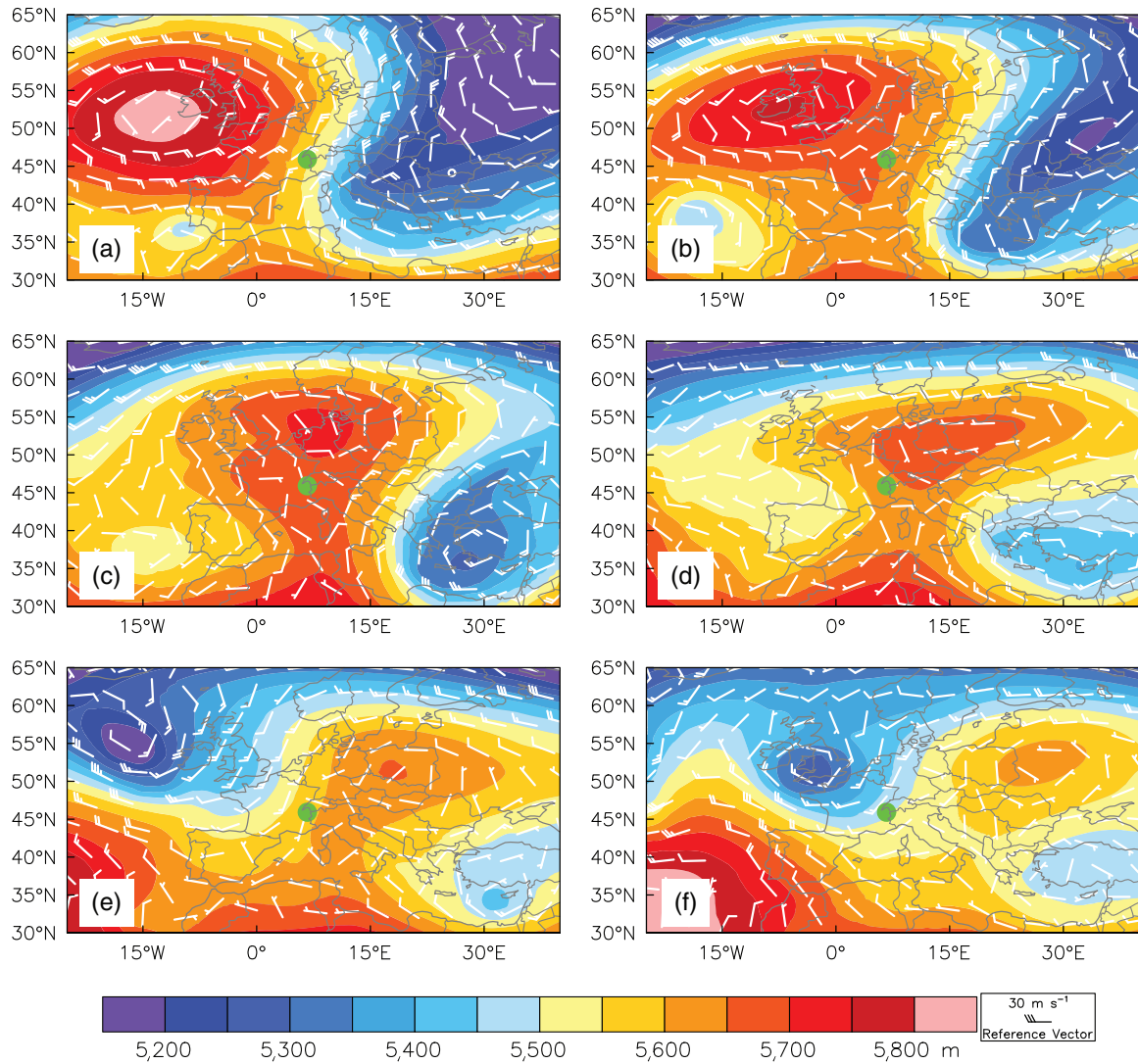


**FIGURE 2** Synoptic weather conditions at 0000 UTC from 9 to 14 February 2015 (a–f) extracted from the European Centre for Medium-range Weather Forecasts (ECMWF) gridded analyses with a horizontal grid point spacing of 0.25°. The coloured contours indicate geopotential height at 500 hPa and wind barbs indicate the wind at 700 hPa. The green dot in the centre indicates the position of the Passy Valley

A set of semi-idealised numerical simulations was performed to extract the effects of the large-scale flow (simulation WRF-I). WRF-I differs from WRF-R in that the domain is twice as large (Figure 1a), and that at the initial time the temperature and humidity fields are horizontally homogeneous and the wind speed is set to zero. The use of a larger domain in WRF-I compared to WRF-R was necessary to minimise spurious effects at the lateral boundaries, at which the normal velocity is set to zero. Hence, the main difference between WRF-I and WRF-R lies in the absence of large-scale flow for WRF-I. The latter simulation was run for the period between 1200 UTC on 10 February and 1200 UTC on 12 February and re-initialised at 1200 UTC on 11 February 2015. The initial temperature and humidity profiles for WRF-I were extracted from the real-case simulation for d04 at the centre of

the domain at the time at which WRF-I was initialised, namely at 1200 UTC on 10 and 11 February 2015. The skin temperature was initialised by extrapolating the temperature of the first three air layers above the ground surface.

### 3 | OVERVIEW OF THE LARGE-SCALE CIRCULATION DURING IOP1

The PCAP that formed in the Passy Valley during IOP1 was the result of the passage of an upper-level ridge over the region. The geopotential height at 500 hPa showed a dipole pattern over Europe between 2 and 8 February 2015, characterised by an upper-level ridge adjacent to a trough. The

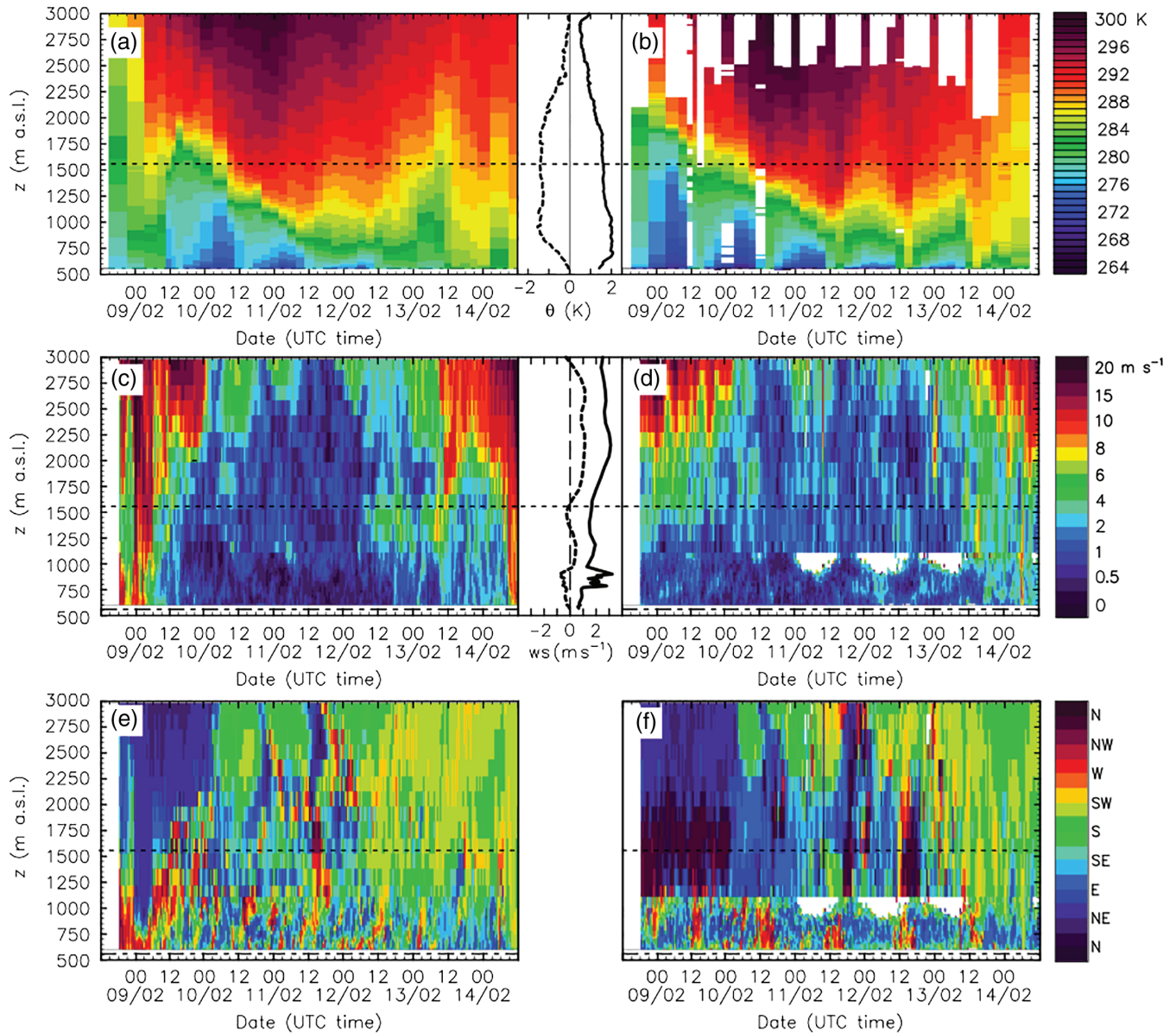


**FIGURE 3** Temporal evolution of the vertical structure of the cold-air pool as obtained from (a, c, e) the WRF-R simulation and (b, d, f) observational data. (a, b) Potential temperature, (c, d) wind speed (ws), and (e, f) wind direction. The potential temperature data are obtained from the radiosonde (RS) ascents, the wind speed and wind direction are retrieved from the LiDAR (below 1050 m a.s.l.) and the wind profiler (above 1050 m a.s.l.) at the RS site during IOPI. The horizontal dashed lines indicate  $z_m = 1560$  m a.s.l. (Figure 1c). The RS site is shown in Figure 1b. The central panels display the root-mean-squared errors (continuous line) and bias (dashed line) of potential temperature  $\theta$  (top row) and wind speed ws (middle row), with respect to observations

upper-level ridge of the dipole pattern was located immediately to the west of the British Isles at 0000 UTC on 9 February 2015 (Figure 2a). The PCAP formed in the evening on 9 February 2015, when the upper-level ridge moved over Northwest Europe (Figure 2b). This synoptic flow pattern led to the advection of warmer air above the western Alps, setting the conditions for the PCAP to develop in the Passy Valley. From 10 to 12 February 2015, the upper-level ridge continued to move across Europe and was centred over Central Europe on 12 February 2015. The displacement of

the ridge resulted in a weakening of the wind speed and a veering of the wind with time over the western Alps from northeasterly on 9 February to southeasterly on 12 February 2015 (Figure 2b–d), allowing the CAP to persist over time. On 13 February the trailing upper-level trough moved across Northwest Europe, leading to a southerly flow and an increase in wind speed over the western Alps (Figure 2e). On 14 February 2015 a large-scale perturbation reached the western Alps (Figure 2f), thereby removing the PCAP and putting an end to IOPI.



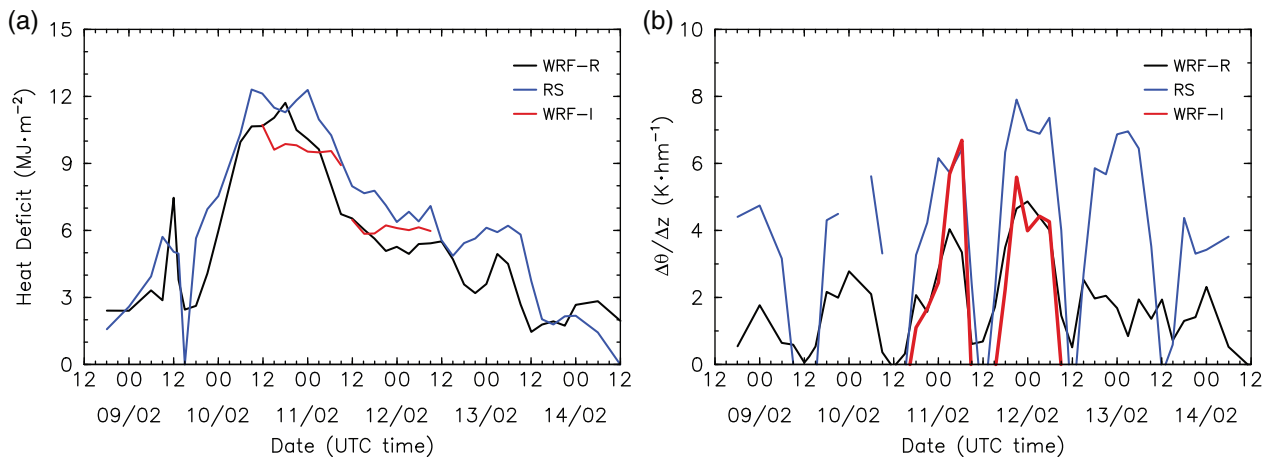


**FIGURE 4** Timeseries of (a) the valley heat deficit, vertically integrated from the ground surface to the mean height of the terrain  $z_m = 1560$  m a.s.l., and (b) the near-surface potential temperature gradient over the lowest 100 m above the surface, at the RS site (Figure 1b), derived from data from the radiosonde ascents and computed from the WRF-R and WRF-I outputs

## 4 | LIFE-CYCLE OF THE PERSISTENT COLD-AIR POOL DURING IOP1

### 4.1 | Vertical structure of the cold-air pool

Figure 3 shows the temporal evolution of the vertical structure of the PCAP obtained by compiling potential temperature profiles from the radiosonde ascents and wind profiles retrieved from LiDAR and wind profiler data at the RS site during IOP1, and extracted from the WRF-R simulation. The temporal evolution is overall well captured in WRF-R. However discrepancies can be noted, in particular before the PCAP event during the night from 8 to 9 February 2015 and at the end of the episode on 14 February 2015 when the simulated temperature and wind speed are overestimated above  $z_m$ . Vertical profiles of the root-mean-squared-error (RMSE) and bias of potential temperature and wind speed between 1200 UTC on 9 February to 1200 UTC on 13 February are also displayed to quantitatively evaluate the numerical results of the simulations. Results before 1200 UTC on 9 February were not included in the computation of the statistics, because the simulation in the outer domain d04 was not fully spun up yet for these times. Statistics for the wind direction are not displayed as, at low wind speeds, the fluctuations of this quantity are large, leading to large RMSE values (Chow *et al.*, 2006). The RMSE of the potential temperature averaged between the valley floor and  $z_m$  is about 1.6 K, decreasing above  $z_m$  to about 1 K. The value of the bias is  $-0.32$  K averaged between the valley floor and  $z_m$ , indicating a slight systematic underestimation of the potential temperature in the simulated PCAP above the valley floor. This statistical

analysis indicates that the model is able to represent the temporal variability of the observed temperature. Regarding the wind speed, the model shows a near-zero bias compared to observations between the valley floor and  $z_m$ , whereas the RMSE is between 1 and  $2\text{ m}\cdot\text{s}^{-1}$ .

The PCAP formed in the evening of 9 February 2015, when warm air was advected above the Passy Valley as the upper-level ridge approached the western Alps (Section 3). Note the weakening and veering of the flow associated with the passage of the ridge (Figures 3c–f and 2). The formation of the PCAP led to a rapid increase of the vertically integrated valley heat deficit (VHD; Whiteman *et al.*, 1999) from 3 to  $12\text{ MJ}\cdot\text{m}^{-2}$ , which is well reproduced in WRF-R (Figure 4a).

Between 1200 UTC on 9 February 2015 and 1200 UTC on 12 February, the structure of the PCAP in the Passy Valley varied substantially, while the wind speed below 2,500 m a.s.l. was of the order of a few metres per second. During this period the height of the PCAP decreased gradually with time, as did the VHD. This decrease was most rapid during the night from 10 to 11 February, by  $4\text{--}5\text{ MJ}\cdot\text{m}^{-2}$ . Although the VHD kept decreasing with time, the night-time near-surface potential temperature gradient computed over the lowest 100 m above the valley floor,  $\Delta\theta/\Delta z_{100}$ , was found to increase from day to day (Figure 4b). This behaviour is well reproduced in WRF-R, but with an underestimate of its amplitude. The different behaviour of VHD and  $\Delta\theta/\Delta z_{100}$  suggests that a thermal decoupling between the near-surface atmosphere and the atmosphere aloft occurs, which will be analysed in detail in the following Sections. The maximum value of  $\Delta\theta/\Delta z_{100}$  was found at 0000 UTC on 12 February as a result of the continuous advection of warm air within the valley atmosphere below  $z = z_m$ .

On 13 February the wind speed in the valley atmosphere increased above  $5 \text{ m}\cdot\text{s}^{-1}$  as a large-scale perturbation approached the western Alps (Section 3). On 14 February the wind speed increased also at the valley bottom, leading to mixing and the full destruction of the PCAP.

## 4.2 | Regional-scale circulation

A more detailed account of the interplay between the local (valley-scale) flow and the regional-scale flow at  $z = z_m$ , simulated in domain d04, is given in Figure 5. Timeseries of wind and temperature at selected sites in the Passy Valley, RS and DS, and in the main tributary valleys, MGV and CHMNX (Figure 1b for the location of the sites), are displayed in Figure 6 to show the response of these fields (in WRF-R) to the large-scale flow.

At 0000 UTC on 10 February 2015, the northeasterly large-scale flow was channelled through the downstream part of the Passy Valley, and split between CHMNX and MGV at  $z = z_m$  (Figures 5a and 6e). Warm air advection occurred overnight across the entire region, where potential temperature  $\theta$  at  $z = z_m$  increased by 7 K in 12 hr (Figure 6f), while it decreased by 2–3 K at  $z = 1,000 \text{ m a.s.l.}$  (Figure 6i). This process, i.e. warming at mid levels and cooling at lower levels, led to the initial strengthening of the PCAP within the Passy Valley, and is well represented in the numerical simulation. At 1200 UTC, the large-scale flow rotated to a southwesterly direction, reaching a minimum wind speed of less than  $1 \text{ m}\cdot\text{s}^{-1}$  at the different sites (Figure 6a,b). A strong and deep down-valley (northeasterly) wind formed in the Rhone Valley, located northeast of the Chamonix Valley near Sion, which was channelled through the gap that connects the two valleys, strengthening the down-valley (northeasterly) flow at CHMNX (Figure 5b).

Potential temperature  $\theta$  at  $z = z_m$  continuously increased on 10 February 2015, reaching a maximum value at 2100 UTC (Figure 6f), that is when the upper-level ridge just passed over the Passy Valley. This can be inferred by noticing the rotation and weakening of the wind aloft (at  $z = 6,000 \text{ m a.s.l.}$ ; Figures 6b and a, respectively). In the early night between 10 and 11 February, the near-surface flow from MGV reversed to down-valley (southwesterly) as the upper-level ridge moved away from the western Alps, and remained down-valley (southwesterly) until the end of the simulated time period (Figure 6k).

During the night between 10 and 11 February,  $\theta$  at  $z = 1,000 \text{ m a.s.l.}$  increased, while it stayed approximately constant at  $z = z_m$  (Figure 6f,i). The large-scale flow at this time was northeasterly to easterly, i.e., aligned with the Rhone and Chamonix valleys, thereby favouring the channelling of the flow down these two valleys (Figure 5c).

Throughout the night, the large-scale flow slowly rotated clockwise and strengthened as the upper-level ridge moved towards the northeast (Figure 6a,b).

Later, at 1200 UTC on 11 February, the large-scale flow veered to southeasterly, and the resulting channelling through the Swiss Plateau gave rise to a regional southwesterly flow at mid-level (Figure 5d), leading to a channelling of the flow through the downstream part of the Passy Valley. During the night between 11 and 12 February,  $\theta$  at  $z = 1,000 \text{ m a.s.l.}$  and  $z = z_m$  hardly varied (Figure 6f,i), while the near-surface temperature dropped throughout the night, as during the previous night (Figure 6l). During this night the amplitude of the diurnal range of  $\theta$  at  $z = z_m$  is underestimated in WRF-R, but the overall temporal evolution is well captured.

From 10 to 12 February, the near-surface temperature at night was non-homogeneous across the valley floor, as indicated by differences of 4 to 5 K between the DS and RS sites that are approximately at the same height (Figure 6l), while the wind speed there was very weak (less than  $1 \text{ m}\cdot\text{s}^{-1}$  on average during this time period). It is worth noting that simulated near-surface temperatures are slightly underestimated at night, though they fall within the observed range when spatially averaged within a radius of a few hundred metres around the sites (not shown). A cold bias of about 3 K is also present in the afternoon. The errors in the representation of the amplitude of the diurnal cycle of the near-surface temperature over snow-covered surfaces in anticyclonic conditions can be related to issues in the representation of turbulent surface fluxes and conductive heat flux into the snowpack. Between 1200 UTC on 10 February and 1200 UTC on 12 February, the RMSE of near-surface potential temperature, wind speed and direction are 2.9 K,  $0.3 \text{ m}\cdot\text{s}^{-1}$  and  $65^\circ$ , respectively. The values for the potential temperature are comparable to or smaller than the ones reported in previous modelling studies of CAPs and PCAPs (e.g., Pagès *et al.*, 2017). It should be noted that the RMSE of the wind speed and direction are computed on a smaller number of data. As before, the relatively large value of the RMSE of the wind direction can be related to the large fluctuations of this quantity occurring at low wind speeds.

During 13 and 14 February 2015, advection of cold air by the large-scale perturbation led to the destruction of the PCAP, strengthening of the near-surface flow with prevailing southerly winds, and a homogenisation of the temperature across the valley floor (Figures 5g,h and 6l).

The overview of the life-cycle of the PCAP presented above leads to the identification of three main time periods, which correspond to the three stages of a PCAP:

- P1** The formation stage – from 8 to 10 February 2015, when the temperature inversion formed in the Passy

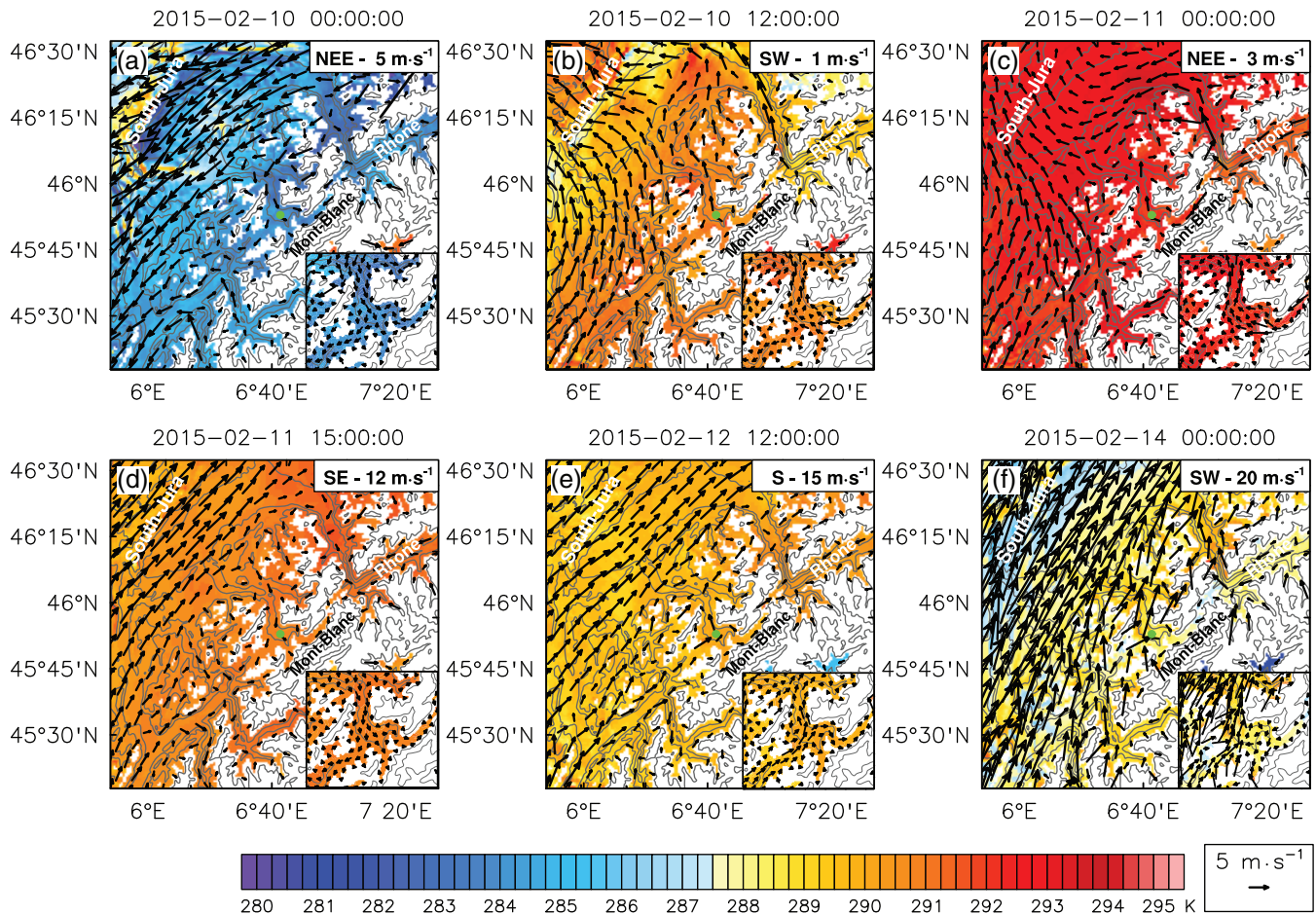


**FIGURE 5** Maps of the wind (vectors), potential temperature (colour shading) and terrain height (grey contours) in domain d04 at  $z = z_m = 1,560$  m a.s.l. at (a) 0000 UTC and (b) 1200 UTC on 10 February, (c) 0000 UTC and (d) 1500 UTC on 11 February, (e) 1200 UTC on 12 February, and (f) 0000 UTC on 14 February 2015. Areas for which the terrain height is above the displayed height level  $z = z_m$  are masked out to better visualise the flow channelling. The speed and direction of the large-scale flow at  $z = 6,000$  m a.s.l. averaged over the RS, DS, MGV and CHMNX sites (Figure 1b shows the locations of the sites) are shown at the top right corner of each plot. The green dot at the centre of each panel indicates the position of the Passy Valley. A zoom on domain d05 is provided at the bottom right corner of each plot

Valley and a change in wind direction was observed aloft;

**P2** The persistent stage – from 10 to 13 February 2015, when the temperature inversion persisted in the Passy Valley;

**P3** The destruction stage – on 14 February 2015.

Since the large-scale flow showed substantial variations with time in wind speed and direction throughout the anticyclonic period, the persistent stage is divided into two sub-periods:

**P2a** From 1200 UTC on 10 February to 1200 UTC on 11 February, when the upper-level ridge moved over the Passy Valley, and the wind speed at  $z = 6,000$  m a.s.l. increased overnight from a minimum value;

**P2b** From 1200 UTC on 11 February to 1200 UTC on 12 February, when the large-scale flow was veering

from southeasterly to southerly, and the wind speed at  $z = 6,000$  m a.s.l. hardly varied with time.

Because the vertical structure and bulk properties of the PCAP show a different behaviour during the two sub-periods of the persistent stage, the link with the variations of the large-scale flow during these periods is analysed in the following sections.

### 4.3 | Valley-scale circulation during the persistent stage

In this section the valley-scale circulation during the persistent stage P2 is described by comparing results from WRF-R and the semi-idealised simulation WRF-I. A mass and heat budget analysis and a mechanistic description

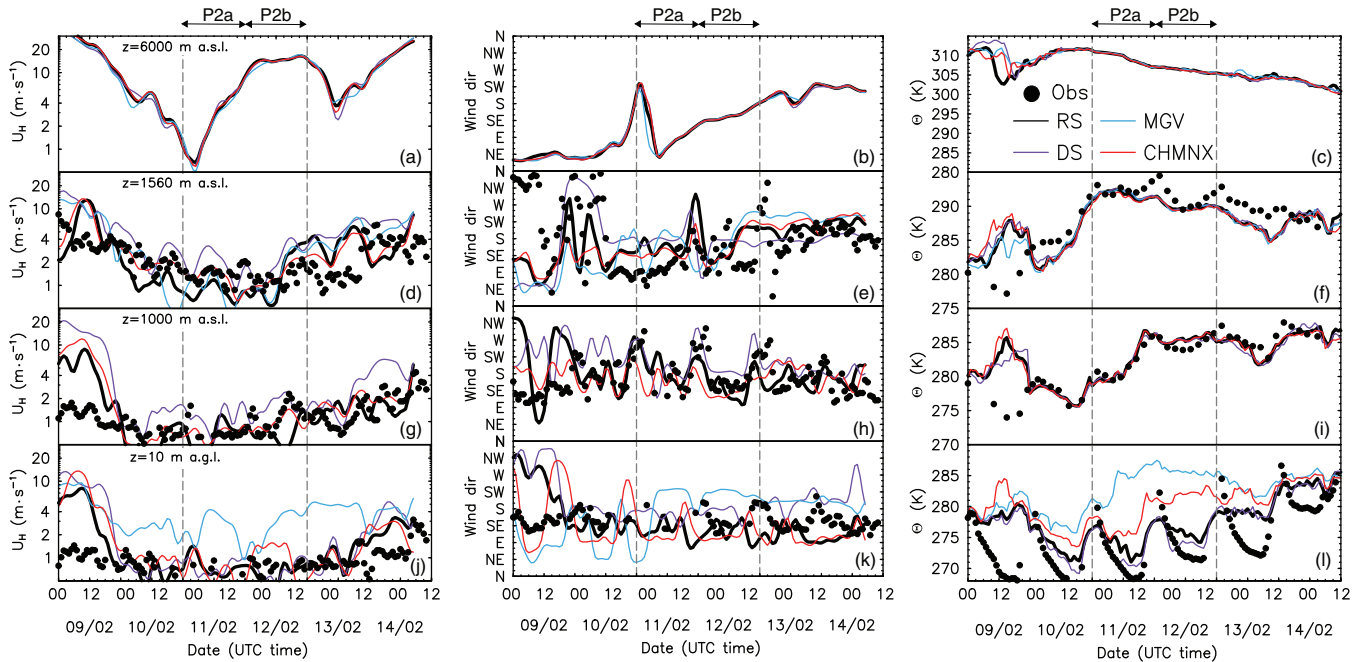


**FIGURE 6** Timeseries of the horizontal wind speed (left column) and direction (middle column), and potential temperature (right column) at  $z=6,000$  m a.s.l.,  $z=z_m=1,560$  m a.s.l.,  $z=1,000$  m a.s.l. and  $z=10$  m a.g.l. (top to bottom rows, respectively), at the RS, DS, MG and CHMNX sites (Figure 1b shows the location of the sites), in WRF-R during the simulated time period. Observational data at the RS site are superimposed as black dots. Wind data are derived from the wind profiler measurements at  $z=z_m$  and  $z=1,000$  m a.s.l. and from an instrumented meteorological mast at  $z=10$  m a.g.l., and potential temperature data at  $z=z_m$  and  $z=1,000$  m a.s.l. derived from the radiosonde measurements and from an instrumented meteorological mast at  $z=10$  m a.g.l. Simulated data at the RS site are shown by a thick black line to facilitate comparison with observations

of the flow behaviour presented in this section will be discussed in Section 5.

#### 4.3.1 | Sub-period P2a

Sub-period P2a (from 1200 UTC on 10 February to 1200 UTC on 11 February 2015) is characterised by a maximum VHD around 1800 UTC, followed by a gradual decrease of the VHD during the course of the night. The wind speed near the surface and at  $z=1,000$  m a.s.l. was at most  $1 \text{ m} \cdot \text{s}^{-1}$  at the different sites considered in Figure 6, except MG, where it was a maximum and of the order of  $3\text{--}4 \text{ m} \cdot \text{s}^{-1}$  near the surface during P2a. The non-local control of the large-scale flow on the near-surface circulation can be extracted by comparing results from WRF-R and WRF-I (Figure 7). Between 1800 UTC and 0600 UTC on the following day, the circulation at the bottom of the Passy Valley is qualitatively similar in WRF-R and WRF-I. There is a clear down-valley flow in the downstream part of the valley and down-valley flows from CHMNX and STGV mostly detach above the valley floor. At the valley exit, the along-valley flow is found to accelerate because

of the narrowing of the valley. The along-valley flow in MG is up-valley at 1800 UTC both in WRF-I and WRF-R, and reverses to down-valley at the surface during the night (Figure 7b,d). However this flow is weaker in WRF-I than in WRF-R, with wind speeds of about  $0.3\text{--}0.5$  and  $3\text{--}4 \text{ m} \cdot \text{s}^{-1}$ , respectively.

The discontinuity in the magnitude of the wind vectors in Figure 7b where the air flows from MG to the Passy Valley indicates that the flow detaches from the surface because of the strong stratification of the PCAP. This detachment is clearly visible in the composite vertical cross-sections which approximately follow the flow (along the white line in Figure 1b), shown in Figure 8. The capping inversion at the top of the PCAP lowers progressively and “sharpens” (i.e., its depth decreases) as the flow through MG strengthens during the course of the night (Figure 8a,c,e). A hydraulic jump forms as the air descends into the Passy Valley (Figure 8e). Conversely, although the flow from MG in WRF-I reverses above the near-surface layer only around 0000 UTC, the upper part of the PCAP cools steadily throughout the night (Figure 8b,d,f), resulting in a deeper PCAP by the end of the night compared to WRF-R. The differences in the flow

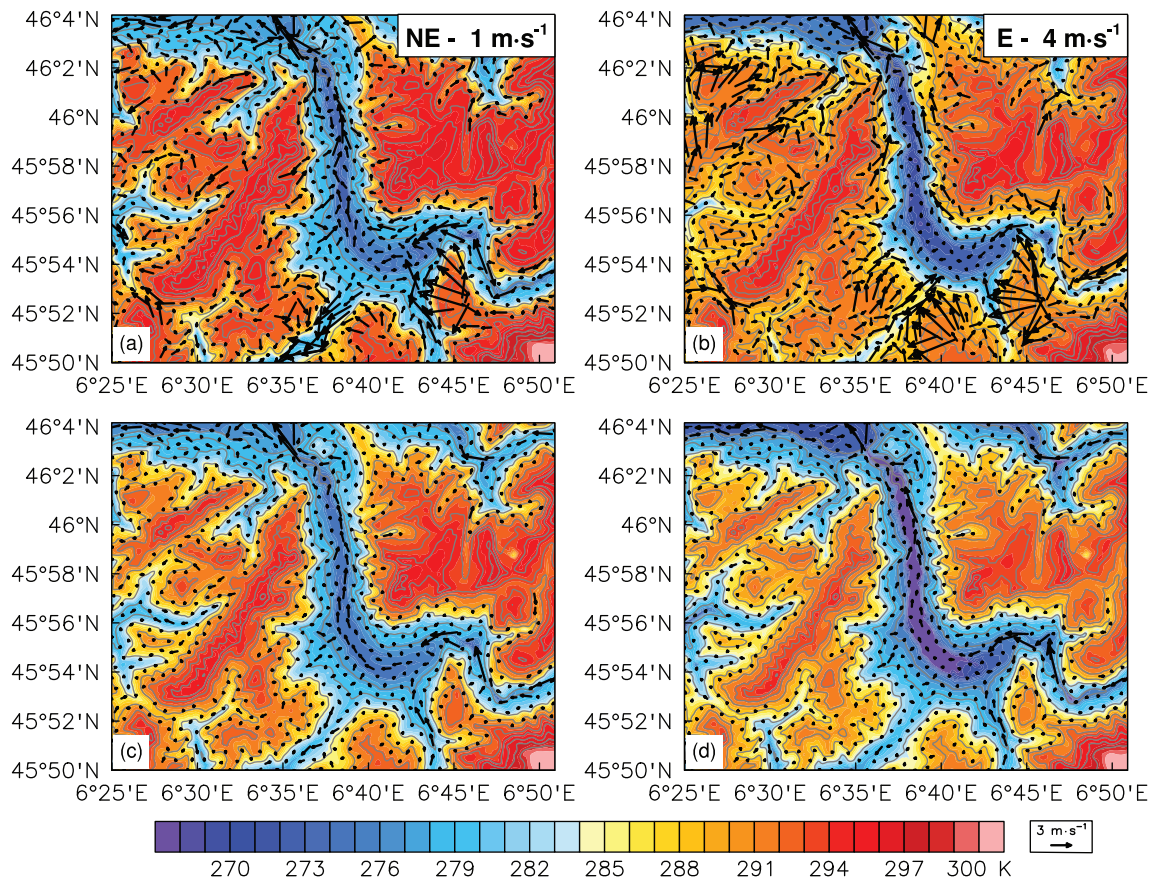


**FIGURE 7** Simulated wind and potential temperature fields at  $z = 10$  m a.g.l. in (a, b) WRF-R and (c, d) WRF-I at (a, c) 1800 UTC on 10 February and (b, d) 0600 UTC on 11 February 2015. The speed and direction of the large-scale flow for WRF-R at  $z = 6,000$  m a.s.l. are shown at the top right corner of the plots

from the tributaries between WRF-R and WRF-I explain the different behaviour of the VHD in the two simulations during the night of P2a (Figure 4a). In WRF-R, the lowering of the PCAP height due to the flow through the tributaries leads to the reduction of VHD throughout the night, whereas in WRF-I the VHD remains about constant with time due to the steady cooling of the atmospheric column.

The lower part of the PCAP displays a temporal evolution of wind speed and thermal structure similar to that in WRF-R, as can be inferred from the isentropes  $\theta = 276$  K in Figure 8. This result suggests that the flow from MGV mostly controlled the increase in temperature around  $z = 1,000$  m a.s.l. between 0000 and 0600 UTC, and more generally the thermal structure of the upper part of the PCAP, while the lower part of the PCAP was mostly controlled by local processes. This will be quantified in Section 5, where the heat and mass fluxes through the tributaries of the Passy Valley atmosphere are analysed.

At 0600 UTC, the near-surface flow in the part of the Passy Valley upstream of RS is weak and almost stagnant

in both WRF-R and WRF-I (Figure 7b,d). However, the near-surface temperature there is lower in WRF-I than in WRF-R, which explains the larger near-surface vertical gradient of potential temperature that develops in WRF-I than in WRF-R during the second part of the night (Figure 4b).

### 4.3.2 | Sub-period P2b

During the sub-period P2b (from 1200 UTC on 11 February to 1200 UTC on 12 February 2015), the evolution of the bulk thermal properties of the Passy Valley atmosphere are more similar in WRF-R and WRF-I than during P2a (Figure 4). At 1800 UTC, the near-surface flows through MGV, CHMNX and STGV are down these tributaries and the near-surface flow in the Passy Valley is down-valley (Figure 9a,c). Hence, the near-surface flow and the flow in the upper part of the PCAP are in opposite directions, i.e., they are dynamically decoupled (Figure 5 and Section 4.2).

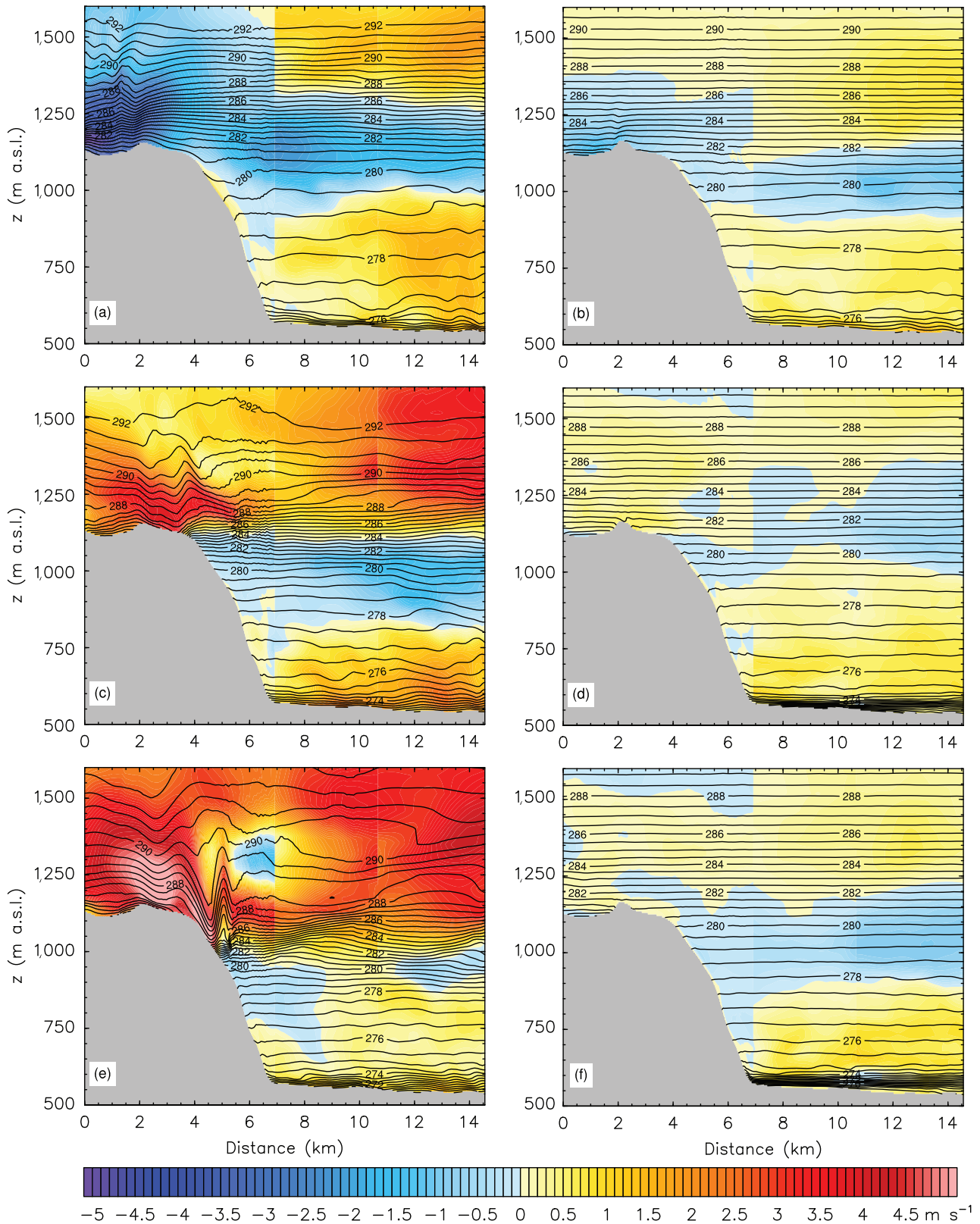


**FIGURE 8** Composite vertical cross-sections following the flow (along the white line in Figure 1b) of horizontal wind speed (in the plane of the cross-section) and potential temperature (K) for (a, c, e) WRF-R and (b, d, f) WRF-I at (a, b) 1800 UTC on 10 February, (c, d) 0000 UTC and (e, f) 0400 UTC on 11 February 2015

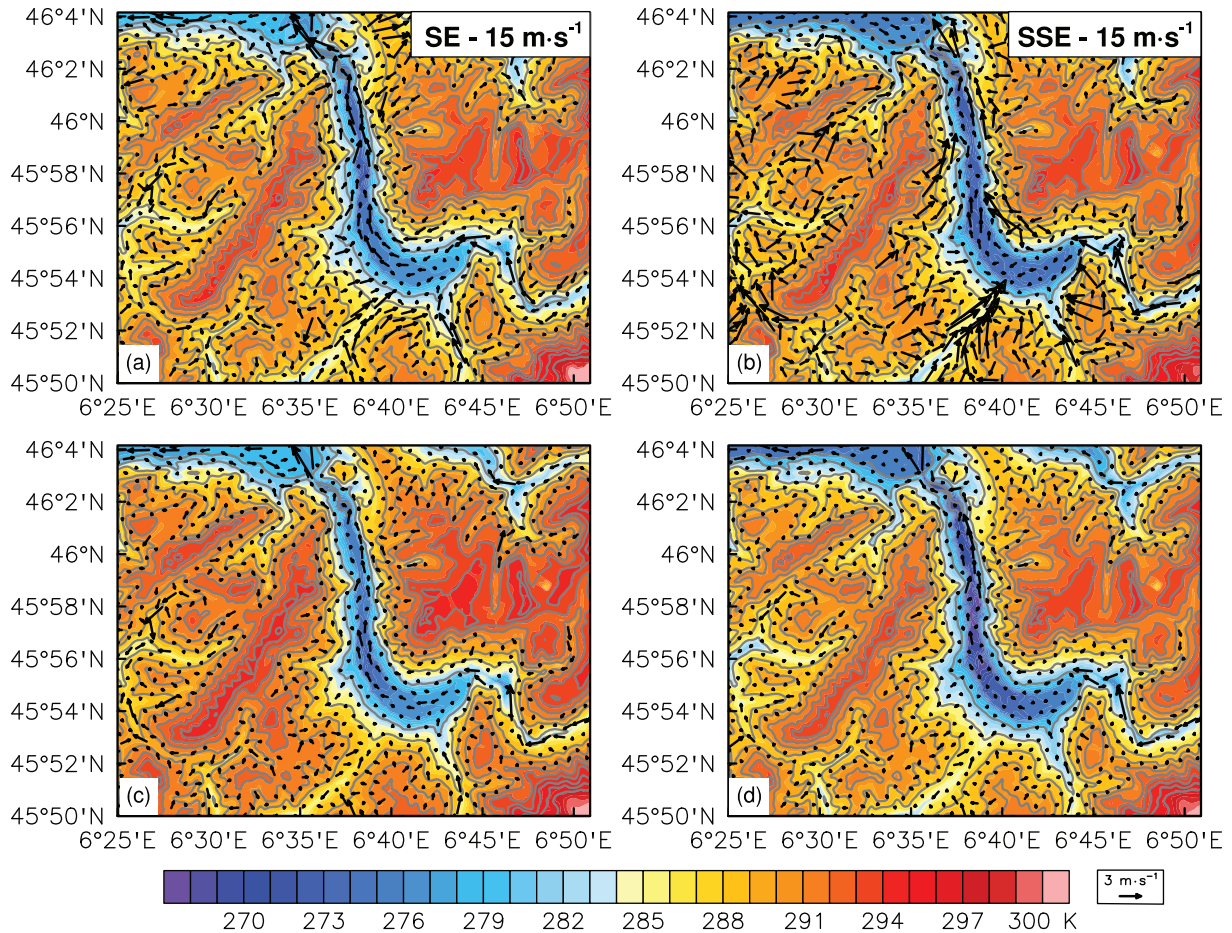


**FIGURE 9** Simulated wind and potential temperature fields at  $z = 10$  m a.g.l. in (a, b) WRF-R and (c, d) WRF-I at (a, c) 1800 UTC on 11 February and (b, d) 0600 UTC on 12 February 2015. The speed and direction of the large-scale flow for WRF-R at  $z = 6,000$  m a.s.l. are shown at the top right corner of the plots

The speed of the flow from MGV increases with time in WRF-R, reaching a maximum value in the morning of 12 February, while it remains constant in WRF-I (Figure 9b,d). The large-scale flow slightly rotates during the night, being more aligned with the MGV valley axis in the morning, suggesting that the increase of wind speed at MGV is an effect of the channelling of this large-scale flow. The flow from CHMNX is weaker than that from MGV and comparable in WRF-R and WRF-I. In contrast to P2a, the near-surface temperature in the Passy Valley is similar in WRF-R and WRF-I during P2b (also Figure 4b).

## 5 | MASS AND HEAT FLUXES THROUGH THE PASSY VALLEY

Section 4.3 highlighted non-local controls of the large-scale flow on the PCAP in the Passy Valley during the persistent stage (P2), in particular in determining the respective contributions of the tributary flows to the mass

and heat budgets of the valley atmosphere. In this section, these contributions are quantified.

### 5.1 | Mass fluxes

The mass budget of the Passy Valley atmosphere is performed over the PASSY control volume, defined in Section 2.1. Assuming incompressibility, the mass budget reads

$$\sum_i \underbrace{\int_{A_i} \rho v_i n_i dS}_{M_i} = M_{DS} + M_{MGV} + M_{CHMNX} + M_{STGV} + M_{TOP} = 0, \quad (1)$$

where  $A_i = A_{DS}, A_{MGV}, A_{CHMNX}, A_{STGV}$ , are the lateral surfaces of the control volume (the blue lines in Figure 1c),  $A_i = A_{TOP}$  is the top surface at  $z = z_m$ ,  $\rho$  is the air density,  $v_i$  is the wind component normal to the surface  $A_i$  orientated

by the unit vector  $n_i$  (defined positive outwards).  $M_i = M_{DS}$ ,  $M_{MGV}$ ,  $M_{CHMNX}$ ,  $M_{STGV}$  are the mass fluxes across the surface  $A_i$ . To compute the mass fluxes, the model fields have to be interpolated onto a Cartesian grid. For the vertical mass flux, this can lead to a misrepresented contribution from the slope flows from the terrain surrounding the PASSY control volume. Hence, to take into account these effects, in the following the vertical mass flux is computed as the residual of the mass budget.

### 5.1.1 | Sub-period P2a

As one may expect, DS is the main exit for the air mass within the valley (Figure 10a). During P2a, both CHMNX and STGV contribute an inflow into the valley, while the mass flux through MGV can be in or out of the valley. When averaged during night-time (from sunset to sunrise),  $M_{CHMNX}$  and  $M_{STGV}$  account for 35% and 18% of the total flow of mass out of the valley, respectively. When combined, the flows from these tributaries provide about half of the mass flowing out of the valley at night during P2a. The other half comes from  $M_{MGV}$  and/or  $M_{TOP}$ .  $M_{MGV} > 0$  (outflow) when the upper-level ridge passed over the valley (i.e., when the wind speed aloft decreases to its minimum value; Figure 6a), and subsiding motions at the valley top account for about 40% of the inflow of mass into the valley. As the upper-level ridge moves away from the region (and the wind speed increases at the upper level; Figure 6a), most of the air mass out of the valley flows through DS, and  $M_{TOP}$  decreases continuously while the flow through MGV reverses ( $M_{MGV}$  changes from positive to negative at about 2200 UTC). During the night from 0300 to 0600 UTC, the inflow of mass from MGV exceeds that from CHMNX and STGV, and the total mass originating from the tributaries exceeds that flowing through DS, resulting in an export of mass across the top of the valley volume.

The mass fluxes in WRF-I are one order of magnitude smaller than those in WRF-R (Figure 10b). The night-time-averaged contribution to the total flow of mass out of the valley from CHMNX is smaller in WRF-I than in WRF-R (25% compared to 35%), implying that the down-valley flow at CHMNX in WRF-R is affected by the channelling of the flow from the Sion valley. Overall, the mass flux analysis demonstrates that the large-scale flow controls the magnitude of the tributary flows and allows us to quantify the relative contribution of the latter flows to the total outflow from the Valley during P2a.

### 5.1.2 | Sub-period P2b

During P2b, between 1300 and 2000 UTC, the large-scale flow was channelled over the Swiss Plateau (Figures 6b

and 5d), resulting in a strong inflow into the downstream part of the Passy Valley (Figure 10a). This inflow through DS is mostly balanced by the outflow through MGV and the export of mass across the top of the valley volume.  $M_{DS}$  reverses from negative to positive at 2000 UTC when the large-scale flow rotates to south-southeasterly and so was in the down-valley direction. At this time,  $M_{MGV} > 0$  and  $M_{TOP}$ ,  $M_{CHMNX}$  and  $M_{STGV}$  contribute equally to the total drainage out of the valley through DS and MGV. As the large-scale flow rotates to southerly, the flow at MGV reverses from up- to down-valley and strengthens, leading to a continuous increase of  $M_{MGV}$  after 0000 UTC.  $M_{CHMNX}$  decreases during the course of the night, contributing on average 15% of the total drainage out of the valley, compared to 35% during P2a. Conversely, the night-time-averaged contribution to the total flow of mass out of the valley from STGV is 16% and comparable to that during P2a. This suggests that the flow through STGV is less sensitive to variations in the large-scale flow than those in CHMNX and MGV.

In WRF-I, each tributary contributes about 30% of the total drainage out of the Passy Valley through DS during P2b. Interestingly  $M_{MGV} < 0$  throughout P2b, as opposed to P2a, implying that the vertical structure of the PCAP influences the direction of the flow through MGV. This can be explained as follows. Since the PCAP at 1200 UTC is much shallower than during P2a, and its top is below the height of MGV, there is no horizontal temperature contrast between RS and MGV and hence there is no thermally driven up-valley flow from the Passy Valley to MGV.

### 5.1.3 | Vertical and horizontal structure of mass fluxes

The analysis presented so far is further developed by examining the vertical structure of the mass fluxes through DS. A significant fraction of the total drainage out of the Passy Valley occurs in the upper part of the PCAP as a result of the detachment of the flow from the tributaries (Figure 11a). The mass flux through DS in the lower part of the PCAP is more variable and has a similar magnitude in WRF-R and WRF-I. This suggests that, despite the flow from the tributaries being a major control on the total outflow from the valley, it mainly affects the upper part of the PCAP with only an indirect effect on the lower part. Indeed, the mass flux in WRF-R is characterised by temporal oscillations between outflow (positive) and inflow (negative). Such oscillations are also visible in WRF-I, but only during P2b (Figure 11b). These oscillations can be triggered either by those of thermally driven flows or by internal gravity waves (IGWs) created by the detachment of the flow through the tributaries at the top



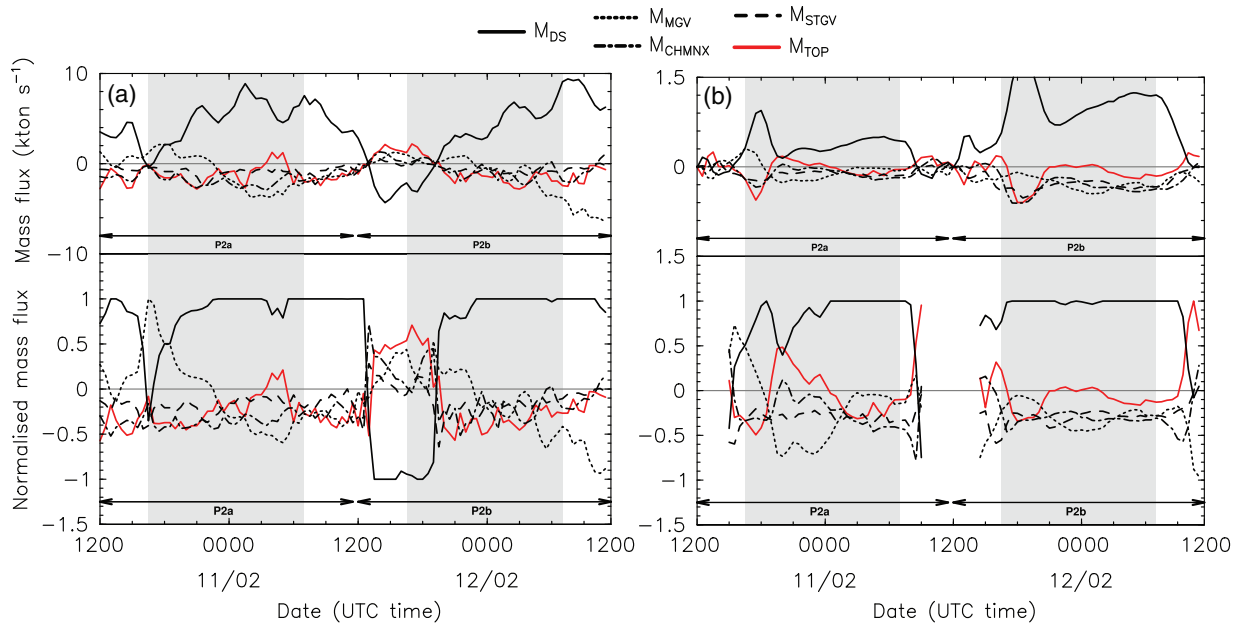


**FIGURE 10** Timeseries of the mass fluxes through DS ( $M_{DS}$ ), MG ( $M_{MGV}$ ), CHMN ( $M_{CHMN}$ ), STG ( $M_{STGV}$ ), vertically integrated from the ground surface to  $z = z_m$ , and through the top surface at  $z = z_m$  ( $M_{TOP}$ ) for the period from 1200 UTC on 10 February to 1200 UTC on 12 February 2015 in (a) WRF-R and (b) WRF-I. Figure 1b,c shows the locations of the gates. The night-time periods (from sunset to sunrise) are shaded grey. The bottom panel shows the mass fluxes normalised by the sum of all mass fluxes out of the Passy Valley (i.e., a positive quantity). Positive and negative values of the mass flux correspond to a flux out of and into the Passy Valley, respectively. Note the different scales in (a) and (b)

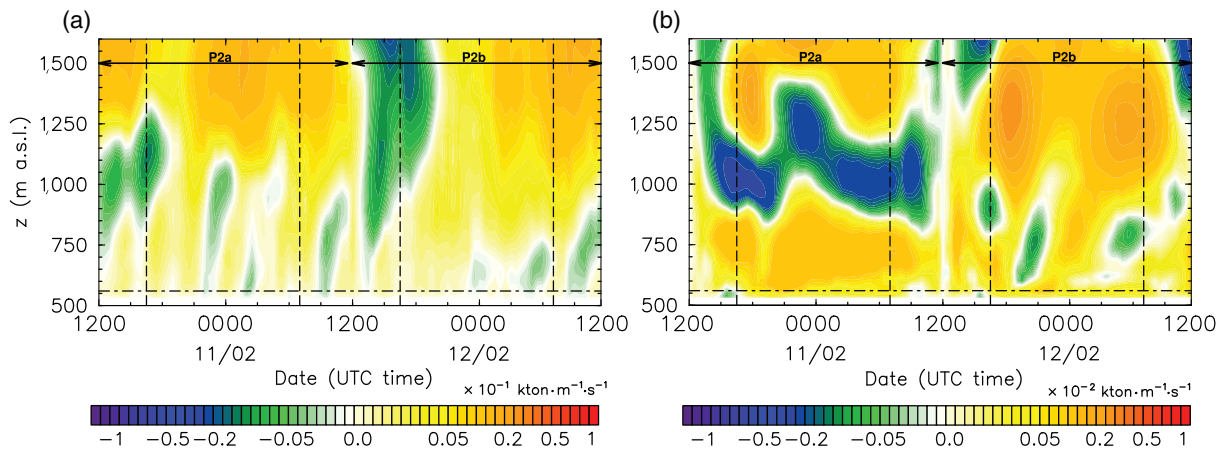


**FIGURE 11** Time–height plot of the mass flux through the downstream (DS) gate for the period from 1200 UTC on 10 February to 1200 UTC on 12 February 2015 in (a) WRF-R and (b) WRF-I. Figures 1b,c show the location of the gate. The night-time periods (from sunset to sunrise) are marked by dashed vertical lines. Note the different scales in (a) and (b)

of the CAP via a hydraulic jump (e.g., Largeron *et al.*, 2013). A closer inspection of Figure 11a,b reveals that the slope of the contours associated with the oscillations with respect to the vertical is non-zero, indicating that there is a phase propagation in the vertical. As a consequence, the hypothesis that oscillations could be triggered by those of thermally driven flows can be rejected, as those are pure oscillations in time with no phase propagation (Largeron *et al.*, 2013; Quimbayo-Duarte *et al.*, 2019). The

horizontal cross-section of the vertical mass flux at the height of STGV during P2a at 2200 UTC confirms the IGW mechanism behind the mass flux oscillations in WRF-R (Figure 12a). In WRF-R the flow through STGV detaches at about  $z = 1,000$  m a.s.l., leading to the formation of IGWs that propagate within the Passy Valley atmosphere. In WRF-I, IGWs are excited by the detachment of the flow from MG and propagate downstream (Figure 12b). A different time period is selected for WRF-I than for

WRF-R because the tributary flows are characterised by different magnitudes and times of occurrence in the two simulations.

## 5.2 | Heat fluxes and impact on the CAP height

The previous subsection revealed the key role of the inflows/outflows from the tributary valleys in the mass budget of the Passy Valley atmosphere during the persistent stage of the CAP and how those flows are affected by the large-scale flow. This section examines their role on the heat budget of the Passy Valley atmosphere.

The heat fluxes are computed from the nonlinear advective term of the volume-averaged density-weighted heat budget equation over the PASSY control volume, i.e., assuming incompressibility,

$$\begin{aligned} \text{ADV} &= \frac{1}{[\text{Mass}]^P} \int_V \rho v_j \frac{\partial \theta}{\partial x_j} dV \\ &= \sum_i \frac{1}{[\text{Mass}]^P} \int_{A_i} \rho (\theta' v_j) n_j dS \\ &= H_{\text{DS}} + H_{\text{MGV}} + H_{\text{CHMNX}} + H_{\text{STGV}} + H_{\text{TOP}}, \quad (2) \end{aligned}$$

where  $[\text{Mass}]^P$  is the mass of the PASSY control volume,  $\theta' = \theta - \bar{\theta}$  and  $\bar{\theta}$  is the volume-averaged potential temperature in the PASSY volume (e.g., Lee *et al.*, 2004), and  $A_i$  the lateral and top surfaces of the volume, defined in Section 5.1.  $H_i = H_{\text{DS}}, H_{\text{MGV}}, H_{\text{CHMNX}}, H_{\text{STGV}}$  are the heat fluxes across the surface  $A_i$ , divided by  $[\text{Mass}]^P$ . The heat flux through the top surface is computed as a residual of Equation (2), as it is done for the vertical mass flux (Section 5.1). In order to quantify the contribution of advective processes to the heat budget of the valley atmosphere, the ADV term above is compared with the volume-averaged density-weighted total tendency, i.e.,

$$\text{TEND} = \frac{1}{[\text{Mass}]^P} \int_V \rho \frac{\partial \theta}{\partial t} dV. \quad (3)$$

TEND is the variation of the heat content of the PASSY volume due to the advection of heat through the lateral and top surfaces of the volume, as expressed in Equation (2), and the vertical divergence of radiative and turbulent heat fluxes. As clear-sky conditions persisted through P2 in WRF-R (except for some sporadic fog that formed near the surface during the night of P2a, not shown), latent heat release/absorption associated with phase changes can be neglected in the heat budget at the valley scale. The effect of the heat fluxes through the tributaries on the thermal structure of the PCAP is evaluated in WRF-R by

investigating the temporal evolution of the CAP height,  $\text{CAP}_h$ , and the bottom height of the capping inversion,  $\text{CI}_h$ .  $\text{CAP}_h$  is defined as the maximum height where the vertical gradient of absolute temperature is positive and  $\text{CI}_h$  is defined as the height where the curvature of  $\theta(z)$  presents a positive maximum. During P2a, when a capping inversion layer exists within the valley atmosphere,  $\text{CAP}_h$  coincides with the top height of this layer, so that the depth of the capping inversion  $d$  can be defined as  $d = \text{CAP}_h - \text{CI}_h$ .

### 5.2.1 | Sub-period P2a

In WRF-R the temporal evolution of TEND during P2 follows that of the advection contribution ADV (Figure 13a). TEND is controlled by ADV during P2a, while it is close to zero during P2b (implying a balance between ADV and the contributions from turbulent heat and radiative flux divergences). The large variations in ADV during P2a are associated with the variability of the advection contributions from the tributaries and top surface of the valley volume. Conversely, in WRF-I the total tendency and advection term have opposite signs and a steady temporal evolution (Figure 13c). Advection contributes to a warming of the valley atmosphere during most of the analysed time period, a behaviour that is typical in synoptically unperturbed conditions as reported in previous studies of idealised CAPs (Schmidli and Rotunno, 2010; Arduini *et al.*, 2017), hence demonstrating the impact of the large-scale flow on the valley heat budget in WRF-R.

A more detailed analysis of the advection contribution in WRF-R reveals the large contribution of tributary flows. In general, the sum of the heat fluxes through MGV, STGV and CHMNX is mostly balanced by an opposite heat flux through DS (Figure 13b). However, the (un)balance between these fluxes varies with time and responds to variations in the large-scale flow, resulting in a net heat input (warming) or export (cooling) from the tributaries, with a large impact on the evolution of the thermal structure of the PCAP. In WRF-I, there is a close balance between the horizontal advection through DS and the vertical advection, with only a minor contribution from the other tributary valleys (Figure 13b).

During the early night until 2200 UTC, the flow through MGV is out of the valley volume (Figure 10a) and  $\text{PCAP}_h$  decreases from  $z = z_m$  to  $z = 1,300$  m a.s.l. (Figure 14a). This is mainly attributed to the warming of the upper part of the PCAP due to subsiding motions across the top surface of the valley volume (70%) and ADV through the other two tributaries, CHMNX and

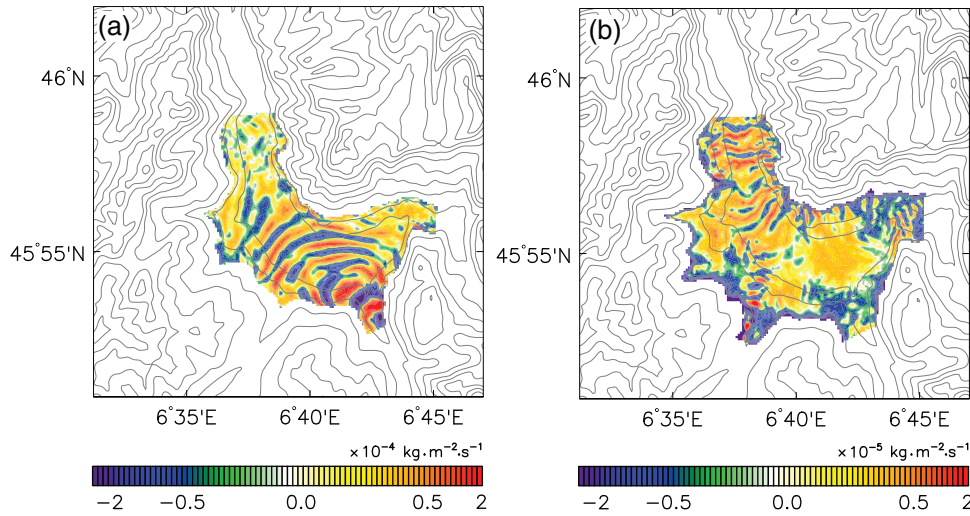


**FIGURE 12** Horizontal cross-sections (across the polygon defining the PASSY volume; Figure 1b) of the vertical mass flux at (a) the height of STGV at 2200 UTC on 10 February (during P2a) in WRF-R and (b) the height of MGVal at 1900 UTC on 11 February 2015 (during P2b) in WRF-I. Positive and negative values of the mass flux correspond to a flux out of and into the Passy Valley, respectively. Note the different scales in (a) and (b)

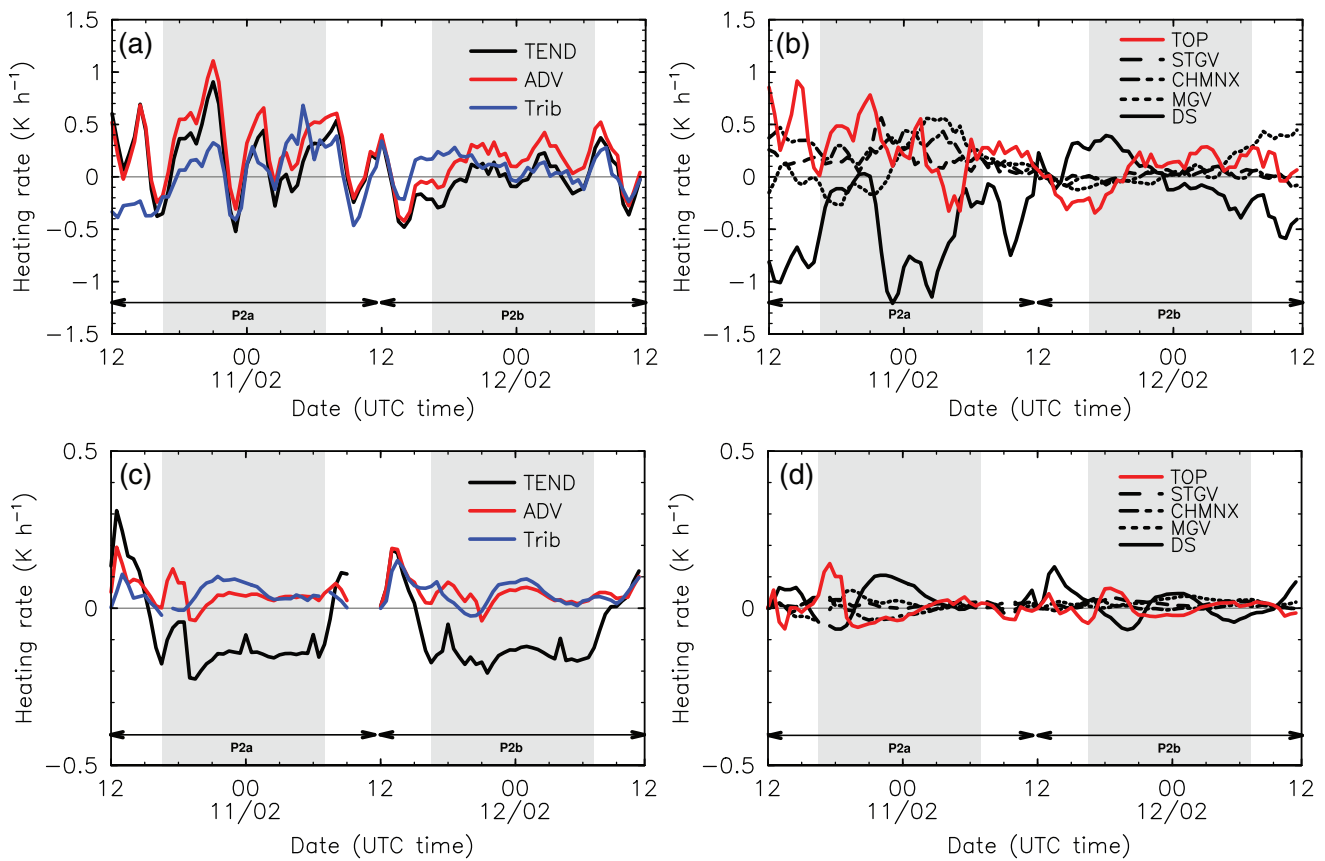


**FIGURE 13** (a) Timeseries of the density-weighted total potential temperature tendency (TEND), advection contribution (ADV) to the total tendency and that restricted to the tributaries (Trib, horizontal advection), averaged over the PASSY volume (Figure 1b), for the period from 1200 UTC on 10 February to 1200 UTC on 12 February 2015 in WRF-R; (b) Timeseries of the horizontal advection contribution to the total tendency from DS, MGVal, CHMNx and STGV in WRF-R (Figure 1b). (c, d) are as (a, b), but for WRF-I. Note the different y-axis scales between (a, b) and (c, d). The night-time periods (from sunset to sunrise) are shown by grey shading

STGV (30%); Figure 13b. This result explains why later on the direction of the flow in MGVal reverses from up-to down-valley. When it is up-valley, that is, flowing from RS towards MGVal,  $CI_h$  is about the height of the valley floor at MGVal and  $d \approx 500$  m (Figure 14b). Hence, the

upper part of the PCAP above the height of the valley floor at MGVal is colder at RS than at MGVal (Figure 14a), leading to a pressure force between the two sites directed out of the valley. As warm air is advected in the upper part of the PCAP, the capping inversion sharpens (i.e.,  $d$

decreases) and the temperature in the upper part of the valley atmosphere becomes higher at RS than at MGV (Figure 14a,b). This chain of processes leads to the reversal of the pressure force, which is then directed into the valley.

As the flow through the tributaries strengthens during the course of the night of P2a, the heat flux through the tributaries increases. From 0200 to 0600 UTC when the mass flux through the tributaries is a maximum (Figure 10a) and  $CAP_h$  and  $CI_h$  decrease continuously with time, ADV is mostly controlled by the heat flux through the tributaries (Figure 13a). The analysis of the heat fluxes together with that of Figure 8, suggest that the upper part of the PCAP is eroded by mixing with the warm air advected through the tributary valleys (mainly MGV after 0200 UTC). Another mechanism that could explain the increase of the potential temperature in the upper part of the PCAP is the downstream displacement of the cold air out of the valley (Lareau and Horel, 2015b). However, the comparison of potential temperature profiles at DS and Marnaz does not show evidence of a downstream displacement (not shown). The advection of warm air leads to a continuous decrease of  $CAP_h$  and  $CI_h$  during the course of the night (Figure 14b), the latter decreasing to 150 m a.g.l. by 0900 UTC. In WRF-I, the CAP height hardly varies with time (not shown) because of the negligible contribution of the advection from the tributary flow to the heat budget at the valley scale (Figure 13d).

### 5.2.2 | Sub-period P2b

During P2b the heat fluxes through the tributary valleys are generally weaker than during P2a (Figure 13b). The capping inversion subsides down to the surface at 1500 UTC, hence leading to a change in the vertical structure of the PCAP. From 1200 to 1500 UTC, the channelling of the large-scale flow into the valley through DS led to a substantial inflow into the PCAP, leading to a heat export (cooling) through the top surface of the valley volume. This heat export results from upward vertical motions induced by the convergence of the tributary flows in the upper part of the PCAP and of the channelled flow through DS. Later, between 1500 and 2000 UTC, turbulent and radiative heat fluxes divergence explain most of the cooling within the PCAP, as the net contribution from advection is close to zero. At 2000 UTC,  $H_{DS}$  and  $H_{TOP}$  change sign, as was the case for the mass fluxes (Figure 10a), becoming negative (cooling) and positive (warming), respectively. From this time until 1200 UTC, ADV is controlled by the interplay between subsiding motions at the valley top and heat fluxes through MGV and DS, which are modulated by the IGW oscillations of the subsiding motions.

## 6 | FACTORS CONTROLLING THE NEAR-SURFACE INVERSION LAYER

During a PCAP episode, thermally driven valley flows are one of the main mechanisms favouring the recirculation of air in the near-surface layer (Quimbayo-Duarte *et al.*, 2019). The basin shape of the Passy Valley constrains horizontal motions in this layer, for which DS is the only gate through which the air mass can flow in and out of the valley. Hence, to investigate the near-surface valley flow, a metric is introduced based on the mass flux through the gate DS (e.g., Whiteman *et al.*, 1996):

$$\tau^{-1} = \frac{M_{DS}^{\Delta z_{100}}}{[\text{Mass}]^{\Delta z_{100}}}, \quad (4)$$

where  $[\text{Mass}]^{\Delta z_{100}}$  is the mass of the PASSY control volume over the lowest 100 m above the valley floor and  $M_{DS}^{\Delta z_{100}}$  is the mass flux through DS, vertically integrated over the lowest 100 m above the valley floor. This height was chosen as it approximately corresponds to the height of the night-time ground-based inversion layer during the persistent stage (Figure 14b). The dimension of  $\tau$  is time, however this parameter is a signed quantity, whose sign depends on the direction of the flow through DS. If  $\tau > 0$ , the flow is out of the valley and  $\tau$  measures the time required to renew the air mass within the PASSY volume below  $z = z_{100}$  through DS. Conversely, if  $\tau < 0$ , the flow through DS is into the valley and the near-surface air is nearly stagnant within the valley, assuming that in very stable conditions, vertical motions at  $z = 100$  m a.g.l. can be neglected.

The parameter  $\tau^{-1}$  is displayed in Figure 15a but, in the following, the behaviour of  $\tau$  is discussed to facilitate its interpretation.  $\tau$  displays temporal oscillations with a period of approximately 3 to 4 hr (Figure 15a), which are the signature of the IGWs excited by the flow through the tributary valleys. As pointed out in Section 5.1, such oscillations are not present during P2a in WRF-I. The amplitude of the oscillations of  $\tau$  in WRF-R is fairly large compared to its mean positive value during both P2a and P2b and makes  $\tau$  vary between positive (outflow) and negative (inflow) values. During P2a, the average value of  $\tau$  over a period of oscillation increases with time during the course of the night and the night-time average is about 7 hr in both WRF-R and WRF-I. The similar trend of  $\tau$  in WRF-R and WRF-I indicates that the near-surface drainage out of the valley is controlled by local thermally driven flows but is modulated by the non-local control of the large-scale flow on the flows through the tributaries. The temporal evolution of  $\tau$  during P2b differs in

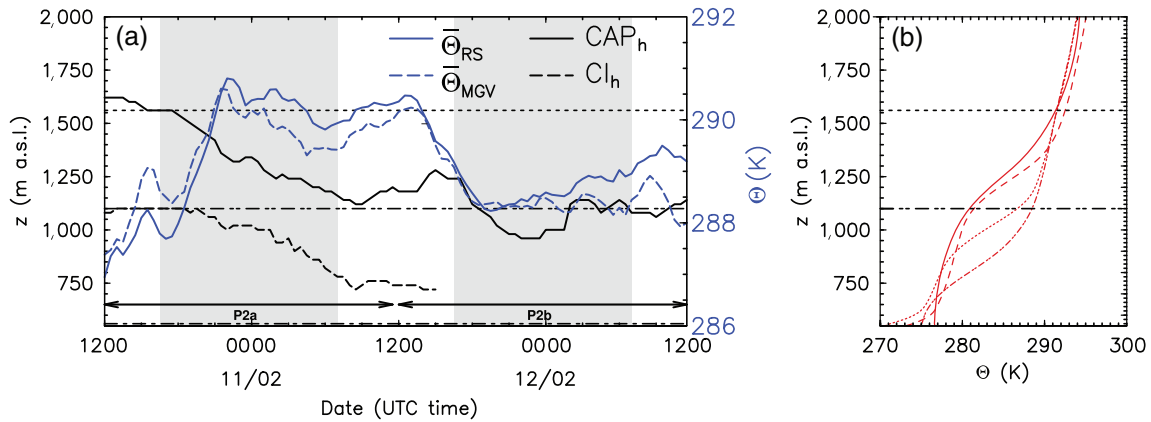


**FIGURE 14** (a) Timeseries of the heights of the cold-air pool ( $CAP_h$ ) and of the capping inversion ( $CI_h$ ), and potential temperature at the RS and MGV sites (Figure 1b), vertically averaged over the height range  $1, 150 < z < z_m = 1,560$  m a.s.l. ( $\bar{\theta}_{RS}$  and  $\bar{\theta}_{MGV}$ , respectively), for the period from 1200 UTC on 10 February to 1200 UTC on 12 February 2015 in WRF-R. The night-time periods (from sunset to sunrise) are shown by grey shading. Note that  $CI_h$  subsides down to the valley floor after 1500 UTC on 11 February; see the text for more details. (b) Vertical profiles of potential temperature at the RS site for selected times during P2a and P2b in WRF-R: 1230 UTC on 10 February (continuous red line), 1930 UTC on 10 February (dashed red line), 0430 UTC on 11 February (dotted red line) and 0900 UTC on 11 February 2015 (dashed-dotted red line). In both panels, horizontal lines indicate the height of the valley floor at MGV (1,100 m a.s.l.) and  $z_m = 1,560$  m a.s.l. (Figure 1c)

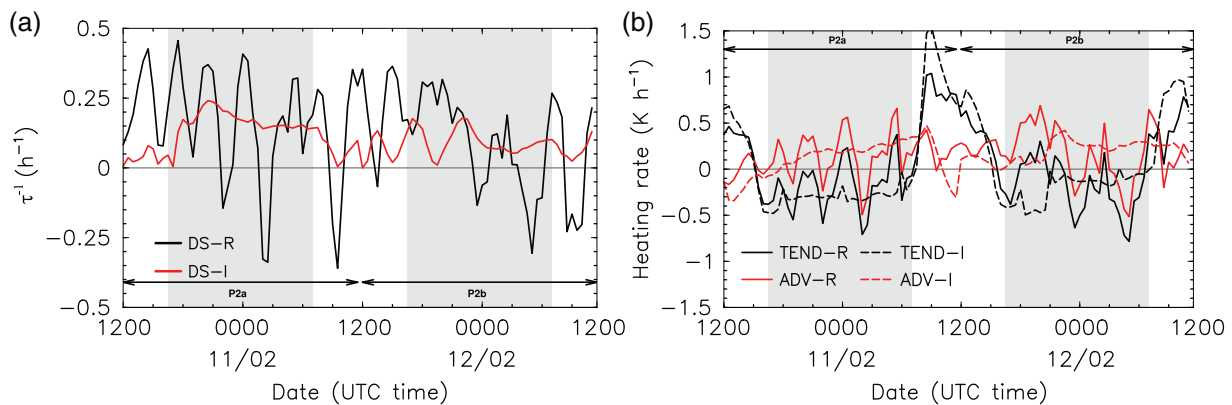


**FIGURE 15** (a) Timeseries of the inverse of the near-surface ( $z < 100$  m a.g.l.) mass turnover time  $\tau$  associated with the mass flux through the downstream (DS) gate (Figure 1b) for the period from 1200 UTC on 10 February to 1200 UTC on 12 February 2015 in WRF-R and WRF-I. (b) Timeseries of the density-weighted total potential temperature tendency (TEND) and advection contribution (ADV) to the total tendency, averaged over the PASSY volume over the lowest 100 m above the ground surface, for the period from 1200 UTC on 10 February to 1200 UTC on 12 February 2015 in WRF-R and WRF-I. The night-time periods (from sunset to sunrise) are shaded grey

WRF-R and WRF-I. In WRF-R the average value of  $\tau$  over a period of oscillation is about 4.5 hr before 2200 UTC and increases to more than 24 hr later. By contrast, the night-time average of  $\tau$  in WRF-I is about 10 hr. This suggests that the non-local control of the large-scale flow is playing a role in the near-surface drainage during P2b in WRF-R.

In order to investigate the impact of non-local processes on the thermal structure of the near-surface atmosphere, the tendency (TEND) and advection (ADV) terms of the heat budget (Section 5.2), averaged over the lowest 100 m over the ground surface, are shown for WRF-R and WRF-I in Figure 15b. The temporal evolution and

magnitude of both TEND and ADV during the morning and evening transitions (0700 to 0900 UTC and 1300 to 1500 UTC, respectively) is similar in WRF-R and WRF-I, indicating that local processes control the heat budget of the near-surface atmosphere during these transition periods. During P2a TEND and ADV display a similar trend in WRF-R and WRF-I during night-time. During P2b, the trends are different: in WRF-R TEND and ADV decrease with time during the night while in WRF-I they increase. Note that, as the consequence of the stagnation of the air mass in WRF-R in the late night during P2b, ADV fluctuates about zero. However, the total tendency integrated throughout the night in P2b is very similar between

WRF-R and WRF-I ( $-5.4$  K and  $-5.8$  K from sunset to sunrise for WRF-R and WRF-I, respectively), implying that, even though the advection contribution varies between the two simulations, the net cooling is hardly affected by the change in the down-valley flow.

This difference between WRF-R and WRF-I during P2b is a result of the evolution of the large-scale flow. The strengthening of the south-southeasterly large-scale flow during the course of the night favours its channelling through MGv in the upper part of the PCAP. The large PCAP stability prevents the channelled flow from penetrating down to the valley bottom, and so enhancing the down-valley flow. The channelled flow transports warmer air in the upper part of the PCAP, so reducing the horizontal temperature difference between the valley centre and outside the valley towards MRNZ (Figures 13a and 16a). This results in a reduction in the near-surface pressure difference driving the down-valley flow between RS and MRNZ between 2100 and 0000 UTC (Figure 16a), leading to the stagnation of the near-surface air within the valley. This non-local effect is not present in WRF-I, which accounts for the near-surface pressure difference continuing to drive a down-valley flow throughout the night (Figure 16b).

## 7 | SUMMARY AND CONCLUSIONS

The purpose of the present work is to examine local and non-local controls on a persistent cold-air pool (PCAP) that formed in the Passy Valley in February 2015 using numerical model simulations. The effect of the non-local controls on the PCAP was determined by comparing the real-case simulation with a semi-idealised simulation with initial quiescent synoptic conditions.

The Passy Valley is a region of Alpine terrain with steep slopes and three major tributary valleys, Megève, Saint-Gervais-les-Bains and Chamonix (Section 2.1). The numerical model simulations were performed using the Weather Research and Forecasting model at a horizontal mesh size of 111 m, carefully initialised (Section 2 gives details). The simulation results are found to realistically capture features of the PCAP by means of comparison with field observations. The model realistically simulates the magnitude and temporal evolution of the valley heat deficit, as well as the vertical structure of the potential temperature, when compared to the available observations. However, it overestimates the near-surface minimum temperature at night-time, which leads to an underestimation of the magnitude of the temperature inversion over the lowest 100 m.

The CAP formed in the evening on 9 February 2015 as a result of the radiative cooling at the valley floor and

advection of warm air above the Passy valley at the mean height of the terrain surrounding the valley, which set the height of the cold-air pool during its formation stage. The advection of warm air was associated with the passage of an upper-level ridge over the region. The effects of the large-scale flow on the CAP during its persistent stage, from 1200 UTC on 10 February to 1200 UTC on 12 February 2015, was investigated at the valley scale and in the near-surface layer above the valley floor (lowest 100 m).

The analysis of the numerical simulations showed that the mass fluxes at the valley scale through the tributaries are about one order of magnitude larger than in the semi-idealised simulation, which demonstrates the impact of the large-scale flow on the flow through the tributary valleys. The flow through Chamonix and Saint-Gervais-les-Bains valleys can supply up to 50% of the air mass that drained out of the valley during one of the nights of the persistent stage of the CAP. As a consequence, the heat budget at the valley scale differs between the real and idealised simulations: this budget is controlled primarily by the flows through the tributary valleys and the vertical advection at the valley top in the real case. This combination of horizontal and vertical advection modified the height of the PCAP. This led to a change in the direction of the flow in the Megève tributary valley, which substantially modified the dynamics and thermal structure of the Passy Valley atmosphere. The results thus showed that local thermally driven flows alone cannot explain the day-to-day variability of the CAP height.

Conversely, the near-surface atmosphere was found to respond differently depending on the position of the upper-level ridge. When the upper-level ridge passed over the Passy Valley (between 10 and 11 February 2015), the mass and heat budgets computed for a near-surface atmospheric volume were found to be comparable between the real and semi-idealised simulations. This implies that the near-surface atmosphere above the valley floor was nearly decoupled from the upper part of the CAP and controlled by and large by local processes, although the flow was modulated by IGWs generated by the detachment of the flow from one of the tributary valleys. As the upper-level ridge moved away from the Passy Valley (between 11 and 12 February 2015), the large-scale flow strengthened, favouring channelling through the Megève tributary valley towards Passy. This flow transported warmer air (in terms of potential temperature) in the upper part of the PCAP, reducing the thermal gradient in the down-valley direction, while being decoupled from the near-surface atmosphere because of the large PCAP stability. This led to the reduction of the surface pressure difference driving the down-valley flow, eventually leading to stagnant air over the valley floor. This mechanism is not present in the semi-idealised simulation, in which a down-valley flow

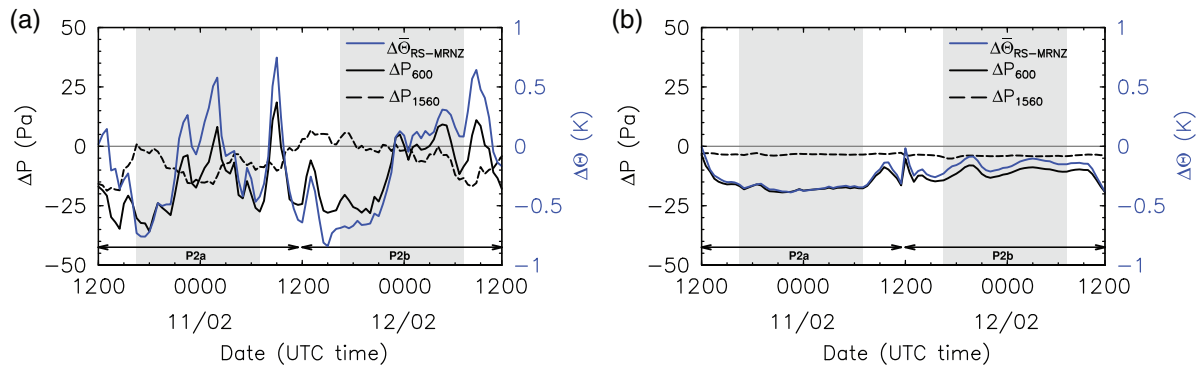


**FIGURE 16** Timeseries of the pressure difference (black lines) between the RS and MRNZ sites (Figure 1b) at  $z = 600$  m a.s.l. ( $\Delta P_{600}$ ) and at  $z = z_m = 1,560$  m a.s.l. ( $\Delta P_{1560}$ ), in (a) WRF-R and (b) WRF-I. Each panel also displays the difference in potential temperature (blue line) between RS and MRNZ sites, vertically averaged in the height range  $600 < z < z_m = 1,560$  m a.s.l. ( $\Delta \bar{\theta}_{RS-MRNZ}$ ). The night-time periods (from sunset to sunrise) are shaded grey

was found to flow out of the Passy Valley throughout the night.

In summary, the main findings of the present work, which are of relevance for other deep Alpine valleys under similar wintertime anticyclonic conditions, are:

- The large-scale flow controls the magnitude of the mass fluxes through the tributary valleys and their relative contribution to the total flow out of the Passy Valley. The flows from the tributaries can contribute more than 50% to this outflow during the persistent stage of the episode.
- The direction of the flow through one of the tributaries is found to be determined by the height of the PCAP with respect to that of the tributary above the valley floor. This result highlights the coupling between the large-scale flow, the tributary flows and the thermal structure of the valley atmosphere during a PCAP event.
- The tributary and large-scale flows modify the heat budget of the valley atmosphere during the persistent stage of the episode, when compared to the heat budget for quiescent synoptic conditions. At the valley scale, the advection contribution is found to be the main control on the total potential temperature tendency.
- Hence, the effect of the non-local controls is key for determining the change in the thermal structure of the CAP from one day to the next, and so the change in the heat deficit. It follows that local thermally driven flows alone are not able to modify the thermal structure of the PCAP on the time-scale of this episode.
- In the present case, the near-surface atmosphere remains almost decoupled from the flow aloft, and two mechanisms are identified. When the upper-level ridge passes over the region, the near-surface atmosphere is subject to usual down-valley flows during night-time; when the ridge moves away from the region,

the near-surface atmosphere become nearly stagnant. This is due to the warm air advection in the upper part of the CAP by the large-scale flow.

The present work calls for a better characterisation of the controls of tributary flows and of varying large-scale flows on cold-air pooling. This would require an approach based on a climatology of the area to identify the prevalence of weather patterns. Future field campaigns should consider instrumenting the main tributary valleys and collecting long-term datasets to sample an extended range of synoptic forcings. Further observations are also required in order to evaluate the role of IGWs in the modulation of the heat and mass budgets of the valley atmosphere. Finally, future modelling studies should also consider the role of fog, and of microphysical processes more generally, in the evolution of a PCAP, as these were not considered in the current work.

## ACKNOWLEDGEMENTS

This work has been supported by a grant from LabEx Osug@2020 (Investissements d'avenir – ANR10LABX56). Numerical model simulations were performed using the UK national supercomputing facilities (ARCHER), accessed through the UK National Centre for Atmospheric Science (NCAS). The Passy-2015 field experiment was supported by ADEME through the French national programme LEFE/INSU and by Météo-France. We thank the cities of Passy and Sallanches for their kind support. The field experiment was led by CNRM while the LEGI laboratory was the principal investigator of the LEFE/INSU project. The rawinsonde data used in Figure 3 are managed by SEDOO at Observatoire Midi-Pyrénées. We thank the people involved in the launching of the rawinsonde and data acquisition therefrom.

## ORCID

G. Arduini  <https://orcid.org/0000-0002-6564-1699>

## REFERENCES

- Arduini, G., Chemel, C. and Staquet, C. (2017) Energetics of deep alpine valleys in pooling and draining configurations. *Journal of the Atmospheric Sciences*, 74, 2105–2124
- Arduini, G., Staquet, C. and Chemel, C. (2016) Interactions between the nighttime valley wind system and a developing cold-air pool. *Boundary-Layer Meteorology*, 161, 49–72
- Billings, B.J., Grubišić, V. and Borys, R.D. (2006) Maintenance of a mountain valley cold pool: a numerical study. *Monthly Weather Review*, 134, 2266–2278
- Bodine, D., Klein, P.M., Arms, S.C. and Shapiro, A. (2009) Variability of surface air temperature over gently sloped terrain. *Journal of Applied Meteorology and Climatology*, 48, 1117–1141
- Burns, P. and Chemel, C. (2015) Interactions between downslope flows and a developing cold-air pool. *Boundary-Layer Meteorology*, 154, 57–80
- Chemel, C., Arduini, G., Staquet, C., Largeron, Y., Legain, D., Tzanos, D. and Paci, A. (2016) Valley heat deficit as a bulk measure of wintertime particulate air pollution in the Arve River Valley. *Atmospheric Environment*, 128, 208–216
- Chen, F. and Dudhia, J. (2001) Coupling an advanced land-surface/hydrology model with the Penn State/NCAR MM5 modeling system, Part I: model implementation and sensitivity. *Monthly Weather Review*, 129, 569–585
- Chow, F.K., Weigel, A.P., Street, R.L., Rotach, M.W. and Xue, M. (2006) High-resolution large-eddy simulations of flow in a steep alpine valley. Part I: methodology, verification, and sensitivity experiments. *Journal of Applied Meteorology and Climatology*, 45(1), 63–86
- Clements, C.B., Archuleta, J. and Gudiksen, P.H. (1989) Experimental design of the 1984 ASCOT field study. *Journal of Applied Meteorology*, 28, 405–413
- Clements, C.B., Whiteman, C.D. and Horel, J.D. (2003) Cold-air-pool structure and evolution in a mountain basin: Peter Sinks, Utah. *Journal of Applied Meteorology*, 42, 752–768
- Coulter, R.L., Martin, T.J. and Porch, W.M. (1991) A comparison of nocturnal drainage flow in three tributaries. *Journal of Applied Meteorology*, 30, 157–169
- Coulter, R.L., Orgill, M. and Porch, W. (1989) Tributary fluxes into Brush Creek Valley. *Journal of Applied Meteorology*, 28, 555–568
- Farr, T.G., Rosen, P.A., Caro, E., Crippen, R., Duren, R., Hensley, S., Kobrick, M., Paller, M., Rodriguez, E., Roth, L., Seal, D., Shaffer, S., Shimada, J., Umland, J., Werner, M., Oskin, M., Burbank, D. and Alsdorf, D. (2007) The Shuttle Radar Topography Mission. *Reviews of Geophysics*, 45. <https://doi.org/10.1029/2005RG000183>
- Flamant, C., Drobinski, P., Furger, M., Chimani, B., Tschannett, S., Steinacker, R., Protat, A., Richner, H., Gubser, S. and Häberli, C. (2006) Föhn/cold-pool interactions in the Rhine valley during MAP IOP 15. *Quarterly Journal of the Royal Meteorological Society*, 132, 3035–3058
- Hall, D.K., Riggs, G.A. and Salomonson, V.V. (2006). MODIS/Terra Snow Cover 5-Min L2 Swath 500m, Version 5, Archived data. NASA National Snow and Ice Data Center Distributed Active Archive Center, Boulder, CO, DOI 10.5067/ACYTYZB9BEOS, (to appear in print).
- Hong, S.Y. (2010) A new stable boundary-layer mixing scheme and its impact on the simulated East Asian summer monsoon. *Quarterly Journal of the Royal Meteorological Society*, 136, 1481–1496
- Jiménez, P.A., Dudhia, J., González-Rouco, J.F., Navarro, J., Mon-távez, J.P. and García-Bustamante E. (2012) A revised scheme for the WRF surface layer formulation. *Monthly Weather Review*, 140(3), 898–918
- Kiefer, M.T. and Zhong, S. (2011) An idealized modeling study of nocturnal cooling processes inside a small enclosed basin. *Journal of Geophysical Research*, 116, D20127. <https://doi.org/10.1029/2011JD016119>
- Lareau, N.P., Crosman, E., Whiteman, C.D., Horel, J.D., Hoch, S.W., Brown, W.O.J. and Horst, T. (2013) The persistent cold-air pool study. *Bulletin of the American Meteorological Society*, 94, 51–63
- Lareau, N.P. and Horel, J. (2015a) Turbulent erosion of persistent cold-air pools: numerical simulations. *Journal of the Atmospheric Sciences*, 72, 1409–1427
- Lareau, N.P. and Horel, J.D. (2015b) Dynamically induced displacements of a persistent cold-air pool. *Boundary-Layer Meteorology*, 154(2), 291–316
- Largeron, Y. and Staquet, C. (2016a) The atmospheric boundary layer during wintertime persistent inversions in the Grenoble valleys. *Frontiers of Earth Science*, 4. <https://doi.org/10.3389/feart.2016.00070>
- Largeron, Y. and Staquet, C. (2016b) Persistent inversion dynamics and wintertime PM10 air pollution in Alpine valleys. *Atmospheric Environment*, 135, 92–108
- Largeron, Y., Staquet, C. and Chemel, C. (2013) Characterization of oscillatory motions in the stable atmosphere of a deep valley. *Boundary-Layer Meteorology*, 148, 439–454
- Lee, T., Fukumori, I. and Tang, B. (2004) Temperature advection: internal versus external processes. *Journal of Physical Oceanography*, 34, 1936–1944
- Livneh, B., Xia, Y., Mitchell, K.E., Ek, M.B. and Lettenmaier, D.P. (2010) Noah LSM snow model diagnostics and enhancements. *Journal of Hydrology*, 11, 721–738
- Lu, W. and Zhong, S. (2014) A numerical study of a persistent cold air pool episode in the Salt Lake Valley, Utah. *Journal of Geophysical Research*, 119, 1733–1752
- McKee, T.B. and O'Neal, R.D. (1989) The role of valley geometry and energy budget in the formation of nocturnal valley winds. *Journal of Applied Meteorology*, 28, 445–456
- Meløysund, V., Leira, B., Høiseth, K.V. and Lisø, K.R. (2007) Review – predicting snow density using meteorological data. *Meteorological Applications*, 14, 413–423
- Mlawer, E.J., Taubman, S.J., Brown, P.D., Iacono, M.J. and Clough, S.A. (1997) Radiative transfer for inhomogeneous atmospheres: RRTM, a validated correlated-k model for the longwave. *Journal of Geophysical Research*, 102, 663–682
- Morrison, H., Curry, J.A. and Khvorostyanov, V.I. (2005) A new double-moment microphysics parameterization for application in cloud and climate models. Part I: description. *Journal of the Atmospheric Sciences*, 62, 1665–1677
- Nakanishi, M. (2000) Large-eddy simulation of radiation fog. *Boundary-Layer Meteorology*, 94(3), 461–493
- Neemann, E.M., Crosman, E.T., Horel, J.D. and Avey, L. (2015) Simulations of a cold-air pool associated with elevated wintertime ozone in the Uintah basin, Utah. *Atmospheric Chemistry and Physics*, 15, 135–151



- O'Steen, L.B. (2000) Numerical simulation of nocturnal drainage flows in idealized valley-tributary system. *Journal of Applied Meteorology*, 39, 1845–1860
- Paci, A., Staquet, C., Allard, J., Barral, H., Canut, G., Cohard, J., Jaffrezo, J., Martinet, P., Sabatier, T., Troude, F., Arduini, G., Burnet, F., Brun, C., Chemel, C., Dabas, A., Donier, J.-M., Garrouste, O., Guillot, R., Langeron, Y., Legain, D., Maurel, W., Tzanos, D., Barrau, S., Barret, M., Barrie, J., Belleudy, A., Bouhours, G., Bourriane, T., Chevrier, F., Douffet, T., Etcheberry, J.-M., Gustave, L., Mazoyer, M., Mercier, S., Moulin, É., Pellan, Y., Pigué, B., Rodier, Q. and Zin, I. (2016) La campagne Passy-2015: dynamique atmosphérique et qualité de l'air dans la vallée de l'Arve. *Pollution Atmosphérique*, 231–232. <https://doi.org/10.4267/pollution-atmosphérique.5903>
- Pagès, M., Pepin, N. and Miró, J.R. (2017) Measurement and modelling of temperature cold pools in the Cerdanya valley (Pyrenees), Spain. *Meteorological Applications*, 24(2), 290–302
- Porch, W.M., Fritz, R.B., Coulter, R.L. and Gudiksen, P.H. (1989) Tributary, valley and sidewall air flow interactions in a deep valley. *Journal of Applied Meteorology*, 28, 578–589
- Quimbayo-Duarte, J., Staquet, C., Chemel, C. and Arduini, G. (2019) Dispersion of tracers in the stable atmosphere of a valley opening onto a plain. *Boundary-Layer Meteorology*, 172, 291–315
- Reeves, H.D. and Stensrud, D.J. (2009) Synoptic-scale flow and valley cold pool evolution in the Western United States. *Weather and Forecasting*, 24, 1625–1643
- Robinson, D.A. and Kukla, G. (1985) Maximum surface albedo of seasonally snow-covered lands in the northern hemisphere. *Journal of Climate and Applied Meteorology*, 24, 402–411
- Schmidli, J., Poulos, G.S., Daniels, M.H. and Chow, F.K. (2009) External influences on nocturnal thermally driven flows in a deep valley. *Journal of Applied Meteorology and Climatology*, 48, 3–23
- Schmidli, J. and Rotunno, R. (2010) Mechanisms of along-valley winds and heat exchange over mountainous terrain. *Journal of the Atmospheric Sciences*, 67(9), 3033–3047
- Sheridan, P.F. (2019) Synoptic-flow interaction with valley cold-air pools and effects on cold-air pool persistence: influence of valley size and atmospheric stability. *Quarterly Journal of the Royal Meteorological Society*, 145, 1636–1659
- Silcox, G.D., Kelly, K.E., Crosman, E.T., Whiteman, C.D. and Allen, B.L. (2012) Wintertime PM<sub>2.5</sub> concentrations during persistent, multi-day cold-air pools in a mountain valley. *Atmospheric Environment*, 46, 17–24
- Skamarock, W.C., Klemp, J.B., Dudhia, J., Gill, D.O., Barker, D.M., Duda, M.G., Huang, X.Y., Wang, W. and Powers, J.G. (2008). A description of the advanced research WRF version 3. Technical Note NCAR/TN-475+STR. NCAR, Boulder, CO.
- Staquet, C., Paci, A., Allard, J., Arduini, G., Barral, H., Barret, M., Blein, S., Brun, C., Burnet, F., Canut, G., Chapuis, D., Chemel, C., Chevrier, F., Cohard, J.-M., Dabas, A., Guyard, H., Jaffrezo, J.-L., Martinet, P., Mercier, S., Mocnik, G., Peinke, I., Quimbayo, J., Sicard, J.-E., Six, D., Troude, F. and Zin, I. (2015). The Passy project: objectives, underlying scientific questions and preliminary numerical modelling of the Passy Alpine valley. In Proceedings of the 33rd International Conference on Alpine Meteorology, 31 August–4 September 2015, Innsbruck, Austria.
- Tomasi, E., Giovannini, L., Zardi, D. and De Franceschi, M. (2017) Optimization of Noah and Noah\_MP WRF land surface schemes in snow-melting conditions over complex terrain. *Monthly Weather Review*, 145, 4727–4745
- Vosper, S.B. and Brown, A.R. (2008) Numerical simulations of sheltering in valleys: the formation of nighttime cold-air pools. *Boundary-Layer Meteorology*, 127(3), 429–448
- Vosper, S.B., Hughes, J.K., Lock, A.P., Sheridan, P.F., Ross, A.N., Jemmett-Smith, B. and Brown, A.R. (2014) Cold-pool formation in a narrow valley. *Quarterly Journal of the Royal Meteorological Society*, 140, 699–714
- Vrhovec, T. (1991) A cold air lake formation in a basin – a simulation with a mesoscale numerical model. *Meteorology and Atmospheric Physics*, 46, 91–99
- Vrhovec, T. and Hrabar, A. (1996) Numerical simulations of dissipation of dry temperature inversions in basins. *Geofizika*, 13, 81–96
- Wei, L., Zhaoxia, P. and Shigong, W. (2013) Numerical simulation of the life cycle of a persistent wintertime inversion over Salt Lake City. *Boundary-Layer Meteorology*, 148, 399–418
- Whiteman, C.D. (1982) Breakup of temperature inversions in deep mountain valleys: Part I. Observations. *Journal of Applied Meteorology*, 21, 270–289
- Whiteman, C.D. (1990). Observations of thermally developed wind systems in mountainous terrain, Chapter 2 in Atmospheric Processes Over Complex Terrain, Blumen, W. (ed.) Meteorological Monographs, Vol. 23, American Meteorological Society, Boston, MA.
- Whiteman, C.D., McKee, T.B. and Doran, J.C. (1996) Boundary layer evolution within a canyonland basin. Part I: mass, heat, and moisture budgets from observations. *Journal of Applied Meteorology*, 35, 2145–2161
- Whiteman, C.D., Bian, X. and Zhong, S. (1999) Wintertime evolution of the temperature inversion in the Colorado Plateau Basin. *Journal of Applied Meteorology*, 38, 1103–1117
- Zängl, G. (2005a) Dynamical aspects of wintertime cold-air pools in an alpine valley system. *Monthly Weather Review*, 133, 2721–2740
- Zängl, G. (2005b) Formation of extreme cold-air pools in elevated sinkholes: an idealized numerical process study. *Monthly Weather Review*, 133, 925–941
- Zängl, G. (2005c) Wintertime cold-air pools in the Bavarian Danube Valley basin: data analysis and idealized numerical simulations. *Journal of Applied Meteorology*, 44, 1959–1971
- Zhong, S., Whiteman, C.D., Bian, X., Shaw, W.J. and M HJ. (2001) Meteorological processes affecting the evolution of a wintertime cold air pool in the Columbia Basin. *Monthly Weather Review*, 129, 2600–2613
- Zhong, S., Bian, X. and Whiteman, C.D. (2003) Time scale for cold-air pool breakup by turbulent erosion. *Meteorologische Zeitschrift*, 12, 229–233

**How to cite this article:** Arduini G, Chemel C, Staquet C. Local and non-local controls on a persistent cold-air pool in the Arve River Valley. *Q J R Meteorol Soc.* 2020;146:2497–2521. <https://doi.org/10.1002/qj.3776>